

Learning Hierarchical Sparse Transform Coding of 3DGS

Hao Xu
McMaster University
xu338@mcmaster.ca

Xiaolin Wu*
Southwest Jiaotong University
xlw@swjtu.edu.cn

Xi Zhang
Nanyang Technological University
xi.zhang@ntu.edu.sg

Abstract

3D Gaussian Splatting (3DGS) supports fast, high quality, novel view synthesis but has a heavy memory footprint, making the compression of its model crucial. Current state-of-the-art (SOTA) 3DGS compression methods adopt an anchor-based architecture that pairs the Scaffold-GS representation with conditional entropy coding. However, these methods forego the analysis-synthesis transform, a vital mechanism in visual data compression. As a result, redundancy remains intact in the signal and its removal is left to the entropy coder, which computationally overburdens the entropy coding module, increasing coding latency. Even with added complexity thorough redundancy removal is a task unsuited to an entropy coder. To fix this critical omission, we introduce a Sparsity-guided Hierarchical Transform Coding (SHTC) method, the first study on the end-to-end learned neural transform coding of 3DGS. SHTC applies KLT to decorrelate intra-anchor attributes, followed by quantization and entropy coding, and then compresses KLT residuals with a low-complexity, scene-adaptive neural transform. Aided by the sparsity prior and deep unfolding technique, the learned transform uses only a few trainable parameters, reducing the memory usage. Overall, SHTC achieves an appreciably improved R-D performance and at the same time higher decoding speed over SOTA. Its prior-guided, parameter-efficient design may also inspire low-complexity neural image and video codecs. Our code will be released at [here](#).

1. Introduction

In recent years, 3D Gaussian Splatting (3DGS) [27] has advanced computer vision and graphics by enabling real-time, high-quality, novel-view synthesis. The cost is substantial storage and bandwidth overheads incurred by storing a very large number of Gaussian primitives, making 3DGS compression an important research topic. Current state-of-the-art (SOTA) methods follow an anchor-based paradigm

that pairs Scaffold-GS [37] with context-based entropy coding to exploit spatial correlations and improve compression ratios [11, 14, 35, 58, 65]. However, these methods forego end-to-end optimized analysis-synthesis transforms that remove redundancy before entropy coding. Without such an analysis transform, high-dimensional correlations persist and the inherent sparsity is left underutilized, forcing complex causal entropy models to compensate for the omission. Yet even large entropy models struggle to accurately capture inter-token dependencies, leading to suboptimal rate-distortion (R-D) performance. Additionally, because the 3DGS compression system operates in the “compress once, decompress many times” mode, decoding speed is critical; using complex entropy models inevitably increases decoding latency and degrades the client-side user experience.

To address aforementioned omission and drawbacks, we integrate an end-to-end optimized analysis-synthesis transform into the 3DGS compression pipeline, thereby removing the most of redundancy before entropy coding. Despite the promise of this paradigm and its maturity in neural image and video compression [6, 15, 32, 41], applying it to 3DGS compression requires overcoming two domain-specific challenges. First, point clouds in 3DGS are unstructured: unlike pixels on a grid, neighboring Gaussians (or anchors) cannot be indexed directly. While K-nearest neighbors (KNN) provides a way to define local neighborhoods on such irregular data, the spatial locations of Gaussians (or anchors) are variables in the R-D optimization and change during training, making per-iteration recomputation of KNN neighborhoods computationally prohibitive. Second, because each scene uses a dedicated transform whose parameters must be transmitted in the bitstream, the parameter budget must remain small; achieving strong performance under this constraint requires careful architectural design.

To tackle these challenges, we propose sparsity-guided hierarchical transform coding (SHTC), which (i) avoids spatial KNN by restricting transforms to channel-wise operations for computational efficiency and (ii) uses a two-layer architecture for parameter efficiency. Layer 1 applies

*Corresponding author.

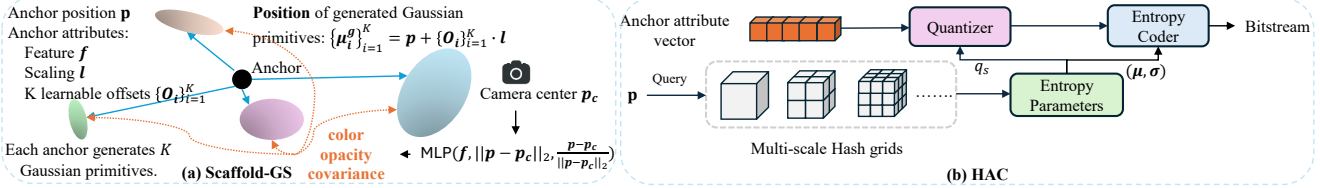


Figure 1. Illustration of Scaffold-GS and anchor-based compression methods.

the Karhunen-Loeve Transform (KLT) for decorrelation and energy compaction, yielding channels with uneven energy distribution. Transmitting only the principal coefficients causes information loss and limits the achievable rendering quality, whereas coding all coefficients is rate-inefficient. To strike a balance between these extremes, we introduce a neural refinement module in Layer 2, which serves as a refinement layer. It compensates for truncation-induced information loss by transmitting the KLT residual with modest additional rate, using a more flexible strategy than direct coefficient coding. Because the residual components are predominantly small (with many values near zero), we model them as sparse. For such sparse signals, compressed sensing theory shows that the full signal can be reliably recovered from a small number of linear measurements rather than coding all coefficients directly [17]. Motivated by this, we design the refinement layer following compressed-sensing principles. At the encoder, the residuals are projected into a low-dimensional latent space via a learnable linear transform that acts as a measurement matrix, and at the decoder they are reconstructed by unfolding the classical Iterative Shrinkage–Thresholding Algorithm (ISTA) [71] into a sequence of network layers [22, 66, 68]. This sparse-recovery-inspired design enables accurate residual reconstruction with low parameter cost.

In conclusion, our key contribution is the introduction of the first end-to-end optimized transform coding framework for 3DGS compression, delivering substantial R-D gains with minimal additional parameters and runtime overhead. Across three standard datasets (Mip-NeRF 360 [7], Tanks&Temples [28], and DeepBlending [25]), our method reduces the memory footprint by 123.5 \times , 216.7 \times , and 705.3 \times relative to vanilla 3DGS, respectively, while matching its rendering quality. In addition, our parameter-efficient design strategy, which combines a sparsity prior with deep unfolding, may offer a potential blueprint for developing low-complexity neural image and video codecs.

2. Related Work

Following the taxonomy of [4], we group existing 3DGS compression methods into (i) unstructured approaches, which employ model compression techniques such as pruning [1, 3, 18, 23, 29, 46] and quantization [20, 44, 57] for

compression, and (ii) structured approaches [31, 37, 42], which exploit the spatial relationship among Gaussian primitives for compression. Because anchor-based designs are especially prevalent within structured approaches and our method builds on this architecture, we dedicate this section to anchor-based methods. Due to space limitations, a more detailed literature review is provided in the supplementary material.

Among anchor-based 3DGS compression methods, Scaffold-GS [37] is the representative baseline. Scaffold-GS introduces a hierarchical structure during training: a sparse set of anchors serve as reference points from which a dense set of Gaussians are generated. As shown on the left side of Fig. 1, each anchor is parameterized by the position p , latent feature f , scaling factor l , and K learnable offsets $\{O_i\}_{i=1}^K$. The scaling factor l together with the offsets determine the spatial distribution of the generated Gaussians. For each generated Gaussian, the view-dependent color, opacity, and covariance (parameterized by quaternion + scale) are predicted from the anchor’s latent feature through lightweight MLPs.

Although Scaffold-GS is more compact than vanilla 3DGS, it is essentially a 3DGS compaction scheme: anchors and their attributes are still stored as raw 32-bit floats without quantization or entropy coding, which inherently limits the achievable compression ratio. SOGS reduces the dimensionality of anchor features; however, this remains 3DGS compaction rather than true compression, so the gains are still limited [67]. To address these limitations, recent work introduces context-based conditional entropy models that reduce statistical redundancy across anchor attributes, achieving significantly higher compression ratios. Among these methods, HAC was introduced early and serves as a foundational baseline. As illustrated in the right panel of Fig. 1, HAC uses multi-scale hash grids as a hyperprior [6]. Given an anchor’s position, it queries these hash grids to obtain contextual features, which an MLP maps to the quantization step size q_s , the Gaussian likelihood parameters (μ, σ) . HAC++ [14] enhances this design by (i) splitting each anchor feature vector into non-overlapping subgroups and encoding them sequentially with a channel-wise autoregressive model (ChARM) [40], and (ii) replacing a single Gaussian with a Gaussian mixture model to model more complex densities. CAT-3DGS [65]

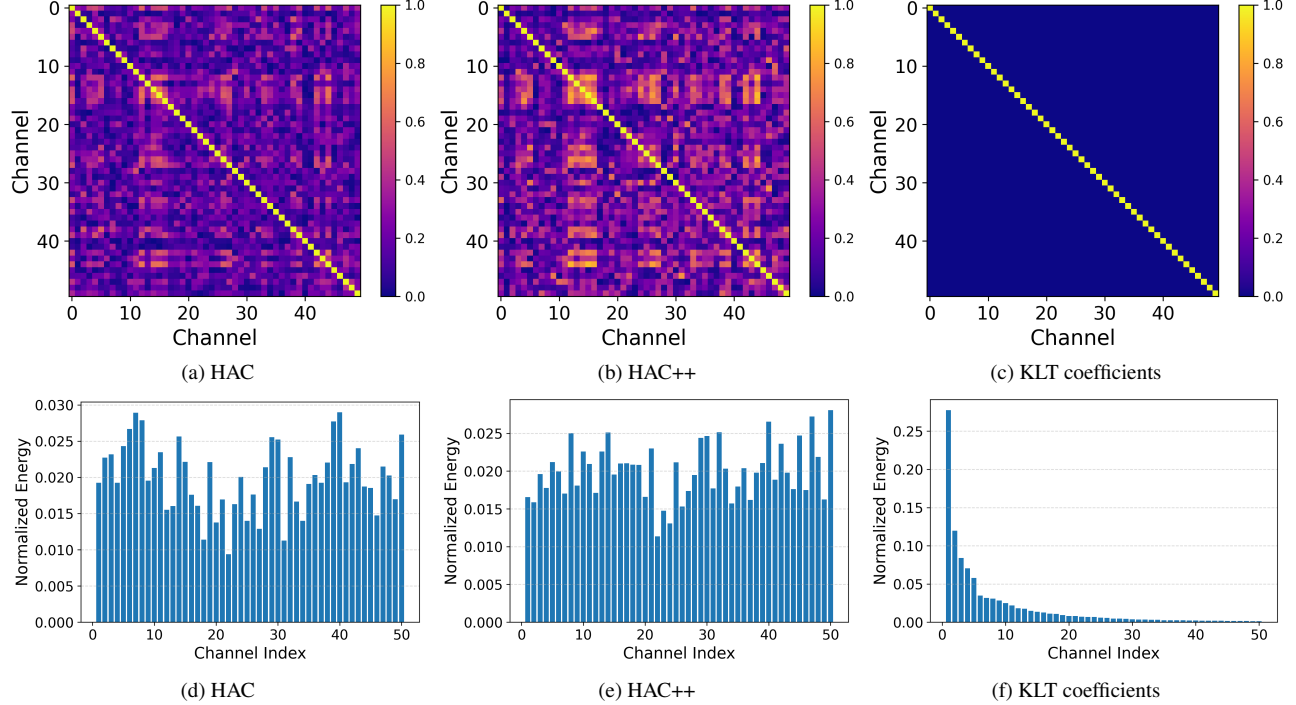


Figure 2. Comparison of inter-channel correlation (visualized as absolute Pearson correlation matrices) and energy compaction in the anchor features of HAC/HAC++ and their KLT coefficients, using the ‘playroom’ scene as an example.

also adopts ChARM but substitutes hash-grid hyperpriors with triplanes. Both ContextGS [58] and HEMGS [35] follow a spatially sequential scheme: they use previously decoded anchors as conditioning context in a spatial autoregressive model (SARM) to encode the next anchors. These approaches represent the current state-of-the-art compression performance for 3DGS compression.

3. Research Motivation and Challenges

In this section, we analyze the importance and challenges of implementing end-to-end optimized transform coding in 3DGS compression.

3.1. Motivation

Decorrelation Anchor-based compression methods, built on Scaffold-GS, achieve high compression ratios by quantizing and entropy-coding anchor attributes. Let \mathbf{x} denote an anchor-attribute vector. With entropy coding, the ideal rate equals the source entropy $H_q = \mathbb{E}_{\mathbf{x} \sim q(\mathbf{x})}[-\log q(\mathbf{x})]$, but the ground truth distribution $q(\mathbf{x})$ is unknown. In practice, one can approximate the unknown distribution $q(\cdot)$ with a parametric model $p(\cdot)$ (often modeled as Gaussian), so the actual rate is the cross-entropy

$$R = \mathbb{E}_{\mathbf{x} \sim q(\mathbf{x})}[-\log p(\mathbf{x})] = H_q + D_{KL}(q||p). \quad (1)$$

where $D_{KL}(q||p)$ measures the extra bits caused by the mismatch between $q(\cdot)$ and $p(\cdot)$. Since anchor attributes are correlated, anchor-based methods use autoregressive models to exploit these correlations and reduce D_{KL} , thereby tightening the cross-entropy rate. For intra-vector correlation, \mathbf{x} can be partitioned into groups of size g and coded sequentially with the probability model $p(\mathbf{x}_{i:i+g}|\mathbf{x}_{<i})$ (e.g., ChARM as used in HAC++ [14] and CAT-3DGS [65]); for spatial correlation, anchors are coded causally with the probability model $p(\mathbf{x}^{(i)}|\{\mathbf{x}^{(j)}\}_{j \in \mathcal{C}_i})$ where \mathcal{C}_i denotes the causal neighbors of anchor- i (SARM as in ContextGS [58] and HEMGS [35]). While more complex entropy models can improve compression by exploiting data correlations during entropy coding, they also increase decoding latency. In 3DGS’s ‘compress once, decompress many times’ pattern, decoding latency on the client side is critical; complex entropy models slow down decoding and degrade user experience. Moreover, even with more complex entropy models, fully capturing these dependencies remains difficult, leading to sub-optimal compression performance. These limitations arise from the absence of end-to-end optimized analysis–synthesis transforms. This motivates introducing such transforms into the compression pipeline: by decorrelating the signal before entropy coding, redundancy is reduced and much simpler, more efficient entropy models can be used. As shown in the first row of Fig. 2, HAC and HAC++ anchor features exhibit strong inter-channel correlations. Ap-

plying a channel-wise KLT largely removes these correlations, yielding decorrelated coefficients and thereby paving the way for the use of simpler entropy models.

Energy compaction In the original signal domain, the relative importance of channels is unclear, hindering efficient rate allocation. After an analysis transform, energy concentrates in a small subset of coefficients, making their importance explicit and enabling more effective rate allocation. This effect is evident in the second row of Fig. 2, where KLT compacts most of the energy into the principal coefficients.

Applying an analysis transform before entropy coding decorrelates the data and compacts its energy, which benefits lossy compression, while a paired synthesis transform reconstructs the anchor attributes for rendering. When the transforms and entropy models are jointly optimized, this transform coding paradigm typically achieves superior R-D performance, as demonstrated in neural image compression [2, 5, 6, 15, 24, 34, 41, 70, 72]. Motivated by these successes, extending this paradigm to 3DGS compression is a natural choice.

3.2. Challenges

Despite the promise of end-to-end optimized transform coding, to the best of our knowledge, no existing work has applied such transforms to 3DGS compression. Extending end-to-end optimized transform coding from neural image compression to 3DGS is, however, non-trivial due to two domain-specific challenges.

The first challenge stems from the irregular, unordered nature of 3DGS anchor points, which lack a natural neighborhood structure. Although neighborhoods can be defined via KNN, repeated neighbor searches in dense point clouds are computationally expensive. This issue is exacerbated by the fact that anchor positions are optimization variables that evolve during training, so the KNN graph must be rebuilt throughout optimization rather than constructed once, significantly increasing the overall training cost.

The second challenge arises from a fundamental difference between 3DGS compression and neural image/video codecs. In standard neural codecs, the analysis–synthesis transforms are trained once, shared across inputs, and omitted from the bitstream; consequently, large-capacity transforms can be used to pursue better R-D trade-offs. By contrast, 3DGS relies on scene-specific transforms whose parameters must be transmitted, imposing a strict parameter budget. Under this constraint, strong R-D performance hinges on architectural efficiency rather than sheer model size. Historically, early neural image codecs with relatively simple transforms [5, 6] failed to surpass traditional codecs, whereas later models with substantially more complex transforms did [15]. This evolution highlights

the difficulty of designing neural transforms that are both parameter-efficient and capable of strong R-D performance.

These two challenges call for careful architectural design to balance R-D gains against additional computational and parameter costs. To address them, we propose SHTC, a transform-coding framework for 3DGS that is both computationally and parameter efficient, achieving strong R-D performance under a tight parameter budget. Technical details of SHTC are provided in Sec. 4.

4. SHTC: Sparsity-guided Hierarchical Transform Coding

In this section, we present our key technical contribution: the first end-to-end optimized transform coding framework for 3DGS compression. We integrate SHTC into HAC [11], replacing the vanilla “quantization→entropy coding” pipeline with a “transform→quantization→entropy coding” pipeline, while retaining Scaffold-GS’s anchor structure and HAC’s computation-friendly entropy model. We first present the architecture of SHTC, using the compression of anchor features as an example. Finally, we present the implementation details of SHTC.

4.1. Layer 1: Base Layer

Transform coding targets decorrelation and energy compaction; among orthonormal linear transforms, KLT is optimal for both. Under a tight parameter budget, we also find that an MLP-based transform lacks the capacity to surpass the KLT. Overall, the KLT offers an excellent cost–performance trade-off, achieving strong R-D performance with minimal compute and memory. We therefore adopt the KLT in Layer 1.

Let $\mathbf{f} \in \mathbb{R}^{N_f}$ denote the anchor feature, with global mean $\mathbf{m} \in \mathbb{R}^{N_f}$ and KLT basis $\mathbf{V} \in \mathbb{R}^{N_f \times N_f}$. The analysis transform is $\boldsymbol{\theta} = g_a(\mathbf{f}) = \mathbf{V}^\top(\mathbf{f} - \mathbf{m})$. The KLT coefficients exhibit an uneven energy distribution. For the anchor feature, we retain only the top- M principal coefficients $\boldsymbol{\theta}_p = \boldsymbol{\theta}_{1:M}$, which are quantized and entropy-coded. The base layer reconstruction is $\hat{\mathbf{f}}_{base} = \mathbf{V}_{:,1:M} \hat{\boldsymbol{\theta}}_p + \mathbf{m}$.

4.2. Layer 2: Refinement Layer via Sparsity-Aware Residual Coding

Discarding the remaining coefficients causes information loss. The artifacts introduced by this truncation become more pronounced at high rates, leading to a quality bottleneck. However, coding all coefficients is rate-inefficient. To mitigate this information loss while keeping the rate overhead modest, we introduce a neural refinement layer. This layer transmits the KLT residual to compensate for truncation. Because most of the signal energy is captured by the leading KLT coefficients, the residual is dominated by low-magnitude components and can be well approximated as

(approximately) sparse. For sparse or compressible signals, compressed sensing theory shows that the full signal can be reliably reconstructed from a small number of linear measurements by solving a sparsity-regularized optimization problem [17]. This insight motivates us to use a principled, sparsity-aware design for the refinement transforms. Instead of relying on a generic multilayer perceptron (MLP), we adopt a parameter-efficient transform inspired by compressed sensing and deep unfolding techniques [66, 68], enabling flexible compression of the residual with low parameter cost.

4.2.1. Analysis Transform: Learned Linear Measurements of Residuals

Let \mathbf{r} denote the KLT residual. We encode \mathbf{r} using a learnable linear analysis transform $h_a(\cdot)$, which projects \mathbf{r} into a lower-dimensional vector $\mathbf{y} \in \mathbb{R}^{N_t}$:

$$\mathbf{y} = h_a(\mathbf{r}) = \mathbf{A}\mathbf{r}, \quad (2)$$

where \mathbf{A} is a learnable matrix. In the language of compressed sensing, \mathbf{A} implements learned linear measurements of the residual. The measurement vector \mathbf{y} is then quantized to $\hat{\mathbf{y}}$ and entropy coded.

4.2.2. Synthesis Transform: Sparsity-Regularized Residual Reconstruction

Given the decoded quantized measurements $\hat{\mathbf{y}}$, the synthesis transform $h_s(\cdot)$ reconstructs an estimate $\hat{\mathbf{r}}$ of the residual:

$$\hat{\mathbf{r}} = h_s(\hat{\mathbf{y}}). \quad (3)$$

Rather than designing $h_s(\cdot)$ as a black-box neural network, we adopt an interpretable formulation that casts residual reconstruction as a sparsity-regularized inverse problem. Assuming that \mathbf{r} admits a sparse representation under a learned dictionary \mathbf{D} , i.e., $\mathbf{r} \approx \mathbf{D}\beta$ with sparse coefficients β , the residual reconstruction can be formulated as the following optimization problem:

$$\tilde{\beta} = \arg \min_{\beta} \frac{1}{2} \|\hat{\mathbf{y}} - \mathbf{A}\mathbf{D}\beta\|_2^2 + \gamma \|\beta\|_1. \quad (4)$$

where the estimation of residual is recovered as $\hat{\mathbf{r}} = \mathbf{D}\tilde{\beta}$.

This inverse problem can be addressed using a variety of well-established optimization algorithms. A classical choice is the Iterative Shrinkage-Thresholding Algorithm (ISTA) [71]. At the k -th iteration, ISTA updates the current estimate by performing a gradient descent step on the quadratic data fidelity term, followed by a soft-thresholding operation to handle the non-smooth ℓ_1 regularization term. The update rule is given by:

$$\beta^{(k+1)} = \mathcal{S}_\tau(\beta^{(k)} - \eta \mathbf{D}^T \mathbf{A}^T (\mathbf{A}\mathbf{D}\beta^{(k)} - \hat{\mathbf{y}})) \quad (5)$$

where η denotes the step size, and $\mathcal{S}_\tau(\cdot)$ is the element-wise soft-thresholding function, defined as $\mathcal{S}_\tau(z) =$

$\text{sign}(z)\max(|z| - \tau, 0)$. Directly applying ISTA, however, can be computationally expensive, as it typically requires many iterations and manual tuning of the hyperparameters τ and η . To address this, we adopt a deep unfolding approach [22, 66, 68] that maps a large number of ISTA iterations to a small number of learnable network layers, significantly reducing inference time while preserving interpretability and the sparsity prior. Each layer corresponds to one unfolded ISTA iteration, with layer-wise learnable step sizes and thresholds. In particular, τ and η are learned separately for each channel in each layer. This design allows the synthesis transform to embed a learnable sparse structure, enabling efficient residual reconstruction from a compact representation with minimal overhead.

Concretely, the synthesis transform $h_s(\cdot)$ takes $\hat{\mathbf{y}}$ as input and initializes the sparse coefficient vector $\beta^{(0)}$. Each unfolded ISTA layer then progressively updates the coefficients as

$$\beta^{(0)} \rightarrow \beta^{(1)} \rightarrow \dots \rightarrow \beta^{(N_s)}, \quad (6)$$

where N_s is the number of ISTA layers. The final predicted residual is recovered as

$$\hat{\mathbf{r}} = \mathbf{D}\beta^{(N_s)}. \quad (7)$$

Finally, the predicted residual $\hat{\mathbf{r}}$ is combined with the base layer reconstruction to form the final anchor feature for rendering.

4.3. Implementation details

There are four types of objects that we need to compress:

- **Anchor positions:** following HAC++ [14], we compress anchor coordinates using MPEG-GPCC [21].
- **Features $\mathbf{f} \in \mathbb{R}^{50}$:** we compress feature vectors with the full two-layer SHTC. The base layer encodes \mathbf{f} into a low-dimensional representation θ_p with $M = 15$. The refinement layer then encodes the KLT residual \mathbf{r} into a measurement vector \mathbf{y} of dimension $N_s = 15$.
- **Scalings $\mathbf{l} \in \mathbb{R}^6$:** for the scaling vectors, we apply only the first SHTC layer (KLT) without dimensionality reduction. Because \mathbf{l} is low-dimensional and the reconstruction quality is highly sensitive to it, truncating KLT coefficients in the transform domain severely degrades performance. Instead, for the KLT coefficients $\mathbf{l}_t \in \mathbb{R}^6$ we adopt a monotonically increasing, channel-wise quantization schedule:

$$q_s^{(i)} = q_s \exp(\alpha i), \quad i \in \{0, \dots, 5\}, \quad (8)$$

where α is a learnable scalar and q_s is the per-anchor base quantization step predicted by HAC. This quantization schedule acts as a remedial measure when dimensionality reduction cannot be applied: it assigns larger steps to lower-energy components, improving the rate-distortion trade-off while avoiding truncation loss.

- **Offsets** $\{\mathbf{O}_i\}_{i=1}^K$: for offset vectors, we retain the original treatment in HAC. Due to offset masking, offset vectors have variable dimensionality across anchors, which makes a fixed transform impractical.

As described in Sec. 2 and illustrated in Fig. 1, HAC uses multi-scale hash grids to parameterize its entropy model. The original HAC queries multi-scale hash grids to predict the quantization step q_s and Gaussian likelihood parameters (μ, σ) for three types of anchor attributes: \mathbf{f} , \mathbf{l} , and $\{\mathbf{O}_i\}_{i=1}^K$. After integrating SHTC into HAC, we slightly modify the entropy coding process. It still queries multi-scale hash grids, but now predicts q_s and (μ, σ) for the transformed vectors θ_p , \mathbf{y} , and \mathbf{l}_t , as well as for the offset vectors $\{\mathbf{O}_i\}_{i=1}^K$. The remaining quantization and coding procedures are the same as in the original HAC.

Inspired by color-space transforms in traditional codecs, we replace the original pixel-wise ℓ_1 loss between the rendered image \hat{I} and ground truth I with a YCbCr-based loss, $\mathcal{L}_{\text{YCbCr}}$, which computes reconstruction errors in the YCbCr color space. Because the human visual system is more sensitive to luminance than to chrominance variations, we assign a higher weight to the Y component and add a sharpness term on Y together with a smoothness term on Cb/Cr to preserve structure while suppressing color noise. This loss regularizes the compressed 3DGS representation, yielding fewer luminance errors and lower perceptual distortion at a given bitrate and thereby modestly improving R-D performance. The full definition of $\mathcal{L}_{\text{YCbCr}}$ is provided in the supplementary material.

The overall training loss is defined as

$$\mathcal{L} = \mathcal{L}_d + \lambda \mathcal{L}_{\text{b-rate}} + \lambda_o \mathcal{L}_{\text{reg}} + \lambda_e \ell_1(\mathbf{r}, \hat{\mathbf{r}}) + \lambda_r \mathcal{L}_{\text{r-rate}} \quad (9)$$

where \mathcal{L}_d denotes the rendering distortion. In practice, \mathcal{L}_d is implemented as a weighted sum of $\mathcal{L}_{\text{YCbCr}}$ and $1 - \text{SSIM}(I, \hat{I})$. The term $\mathcal{L}_{\text{b-rate}}$ represents the estimated bit rate of θ_p , \mathbf{l}_t , and $\{\mathbf{O}_i\}_{i=1}^K$, while $\mathcal{L}_{\text{r-rate}}$ represents the rate of \mathbf{y} . The regularization term \mathcal{L}_{reg} includes the additional loss terms inherited from the HAC framework, and $\ell_1(\mathbf{r}, \hat{\mathbf{r}})$ encourages accurate reconstruction of the residual signal. When estimating the rate during training, we follow HAC++ [14] and take the anchor mask into account.

5. Experimental results

5.1. Experimental setup

Dataset We primarily evaluate the R-D performance on three commonly used large-scale real-scene datasets: DeepBlending [25], Mip-NeRF360 [7], and Tanks&Temples [28]. In particular, we assess all nine scenes from the Mip-NeRF360 dataset [7]. Evaluations on additional datasets are provided in the supplementary material. These diverse datasets provide a comprehensive evaluation of the proposed SHTC framework.

Distortion metrics We evaluate rendering distortion using three metrics: PSNR, SSIM [59], and LPIPS [69].

Rate metrics We adopt the BD-rate metric [8] to quantify memory savings by comparing the R-D curve of a compression method against that of a baseline. Specifically, BD-rate computes the average bitrate difference between the two R-D curves over a common distortion range. A negative BD-rate indicates that, on average, the method achieves a lower bitrate (measured in memory size) than the baseline at comparable distortion levels, with the absolute value (expressed as a percentage) quantifying the average bitrate reduction.

Training details We follow the official training settings of HAC [11] and HAC++ [14], and train each scene for 30k iterations. The Lagrange multiplier λ is set to $\{0.002, 0.004, 0.008, 0.015\}$ to obtain R-D curves that span a wide range of bitrates and distortions for a more comprehensive comparison. The gaps between successive λ values are chosen to increase because the effect of λ on the achieved bitrate is highly non-linear: especially in the low-bitrate regime, larger changes in λ are required to produce clearly separated bitrates and thus more evenly distributed points on the R-D curve. We set $\lambda_e = 0.03$ and $\lambda_r = \max(\lambda/4, 0.001)$. All experiments are conducted on a server equipped with two RTX 4090 GPUs.

5.2. Comparison with Anchor-based Methods

5.2.1. Evaluating R-D performance

Fig. 3 shows the R-D curves of several anchor-based 3DGS compression methods. Across all three datasets, the curve corresponding to the proposed SHTC, labeled “Ours SHTC (Full)” in the legend, lies toward the upper-left region, indicating higher PSNR at a given size or, equivalently, smaller size at a given distortion. For PCGS [12], we train the model with $\lambda \in \{0.004, 0.008, 0.015, 0.025\}$ to span a wide distortion range, so that its R-D points exhibit sufficient PSNR variation and a modest amount of overlap with the other methods, making the differences in the bitrate required to reach a given PSNR clearly visible. For HEMGS [35], which is not open-sourced, we plot the R-D points reported in their paper and conduct an approximate comparison. Using only half as many training iterations (30k vs 60k), our method performs on par with or better than HEMGS on Mip-NeRF360 and DeepBlending and appears competitive on Tanks&Temples.

Tab. 1 reports the corresponding BD-rate of SHTC relative to HAC++, CAT-3DGS, and ContextGS, quantifying the bitrate (memory footprint) savings at equal PSNR. On average over the three datasets, our method achieves BD-rate values of about -21.0%, -24.3%, and -43.6% relative to HAC++, CAT-3DGS, and ContextGS, respectively.

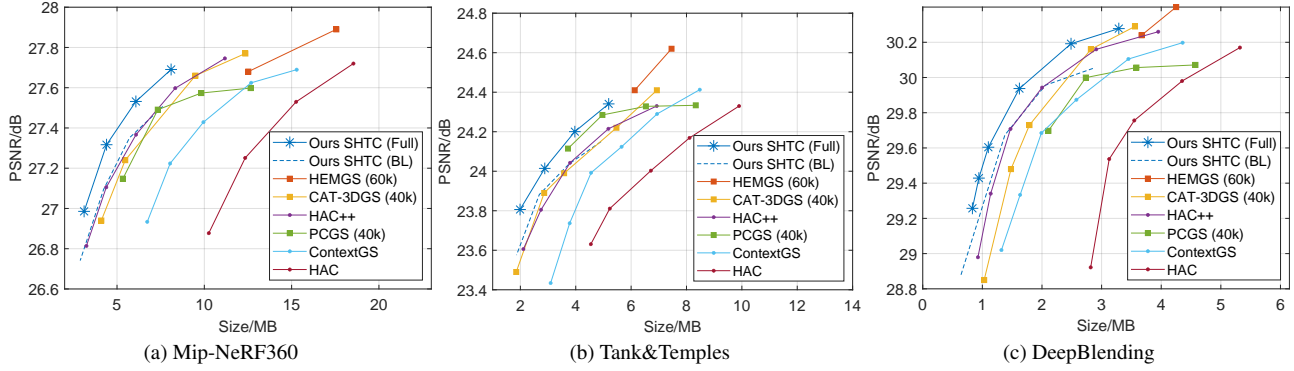


Figure 3. Comparison of our method with existing anchor-based 3DGS compression methods.

Taken together, these results indicate that combining end-to-end optimized transforms with a simple entropy model is more effective than solely increasing entropy-model complexity in anchor-based 3DGS compression. This highlights the importance of incorporating transform coding and demonstrates the strong performance of the proposed SHTC framework.

Dataset	HAC++	CAT-3DGS (40k)	ContextGS
Mip-NeRF360	-20.81%	-24.54%	-49.36%
Tank&Temples	-22.55%	-22.78%	-39.17%
DeepBlending	-19.58%	-25.53%	-42.30%

Table 1. The BD-rate of SHTC relative to three baselines: HAC++ [14], CAT-3DGS [65] and ContextGS [58]. Negative values indicate bitrate savings (better) compared with each baseline.

5.2.2. Evaluating Computational Cost

As shown in Tab. 2, our method not only achieves greater BD-rate gains relative to the HAC baseline than HAC++ and ContextGS, but also reduces both encoding and decoding latency. This efficiency gain stems from a paradigm shift: instead of relying on a highly complex entropy model to capture dependencies among high-dimensional anchor features, SHTC uses learned transforms to explicitly decorrelate anchor attributes before entropy coding. By shifting the decorrelation burden from the entropy model to the transform, SHTC produces coefficients for which a simple and fast entropy model is sufficient, yielding better overall compression efficiency and lower latency than relying on a highly complex entropy model alone.

In terms of training time, SHTC introduces a modest overhead. In our experiments, compared with HAC++, the training time per scene increases by at most about 8 minutes, while HAC++ itself already requires approximately 40–50 minutes to train. However, this additional cost is less critical in practice, because training is a one-time offline cost borne by 3DGS asset producers, whereas decoding is

performed repeatedly on the user side: end users neither observe nor care about the training time, but they are directly sensitive to download and decoding latency. SHTC targets this more critical bottleneck by producing smaller bitstreams at comparable distortion and reducing decoding latency, making it particularly well suited for consumer-centric applications where fast access is essential. A detailed comparison of training times is provided in the supplementary material for reference.

In terms of parameter overhead, the transforms in SHTC introduce 5,093 additional parameters over the HAC baseline. However, when SHTC is integrated into HAC, the entropy model queries the hash grids and feeds an MLP that predicts probability parameters for low-dimensional transform coefficients instead of high-dimensional anchor features. This change reduces the size of this MLP. As a result, the integration of SHTC into HAC incurs a net overhead of only 1,154 parameters. In contrast, HAC++ increases the number of parameters by 45,400 relative to HAC. These results highlight the parameter efficiency of SHTC, which stems from a sparsity-aware transform design rather than simply adopting a larger black-box MLP.

5.2.3. Visual Comparison

Due to space limitations, visual comparisons are provided in the supplementary material.

5.3. Comparison with Other Methods

In addition to the comparisons with anchor-based compression methods using R–D curves and BD-rate, we also evaluate our method against a broad set of anchor-free and hybrid baselines [13, 18, 20, 23, 27, 29–31, 36–38, 42, 42, 44, 45, 47, 51, 53–55, 57, 61, 62, 64]. Because many of these methods only report one or two operating points on the R–D curve, they do not support a meaningful BD-rate computation; for these methods, we therefore provide a numerical comparison in tabular form in the supplementary material.

In the main text, we focus on several conceptually representative baselines: the classic 3DGS [27] and Scaffold-

	Rendering FPS↑			Encoding time (s)↓			Decoding time (s)↓			BD-rate↓		
	ContextGS	HAC++	Ours	ContextGS	HAC++	Ours	ContextGS	HAC++	Ours	ContextGS	HAC++	Ours
Mip-NeRF360	106	128	146	32.73	8.48	5.90	33.32	13.86	8.86	-30.92%	-56.60%	-64.82%
Tank&Temples	130	158	177	29.37	5.63	3.91	29.05	8.81	5.80	-26.41%	-44.87%	-56.06%
DeepBlending	161	169	185	16.78	2.98	2.30	16.63	4.41	3.18	-41.09%	-58.34%	-64.56%

Table 2. Evaluating inference efficiency and compression effectiveness: complex entropy modeling alone vs. SHTC with a simple entropy model. From left to right, we report four metrics: rendering FPS, encoding time, decoding time, and BD-rate relative to the HAC baseline. All results are obtained from models trained with $\lambda = 0.004$. The best result for each metric is highlighted in **bold**.

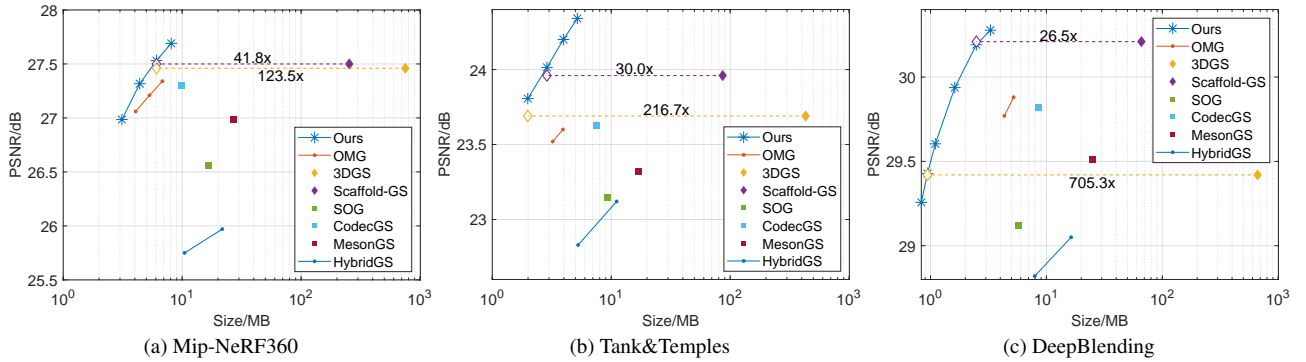


Figure 4. Comparison of our method with several conceptually representative baselines.

GS [37], the current SOTA anchor-free compression method OMG (NeurIPS 2025) [30], and four representative methods that apply transform coding in a post-training stage for 3DGS compression: SOG and MesonGS (ECCV 2024) [42, 61], CodecGS (ICCV 2025) [31], HybridGS (ICML 2025) [64]. As shown in Fig. 4, our method consistently achieves better R-D performance than OMG and significantly outperforms the post-training transform-coding approaches. These results clearly demonstrate that jointly optimize the GS representation and the transforms in an end-to-end manner is substantially more effective than applying a fixed transform after training. Averaged over the three standard datasets in Fig. 4, our method reduces the memory footprint by about $349\times$ relative to vanilla 3DGS and by about $33\times$ relative to Scaffold-GS, while maintaining comparable rendering quality.

5.4. Ablation Study

As shown in Fig. 3, using only the base layer of SHTC, denoted as ‘Ours SHTC (BL)’, achieves slightly better or comparable R-D performance compared to HAC++ at low and medium bitrates. However, the improvements are modest overall, and SHTC (BL) fails to consistently surpass HAC++ in the high-rate region. This limited gain is mainly due to truncation-induced information loss in the base layer, which inevitably discards some useful information and constrains the achievable performance. In contrast, when we use the full SHTC to compress anchor attributes, which includes an additional neural refinement layer to compen-

sate for truncation-induced information loss, the proposed method yields consistent gains over HAC++ across both low- and high-rate regions. At high bitrates, it also remains clearly superior in terms of R-D performance and does not suffer from the high-rate quality bottleneck observed with the base-layer-only variant.

The supplementary material provides a more detailed quantitative ablation study and a further analysis of the choice of transforms, and also discusses the limitations of our approach and directions for future work.

6. Conclusion

In this paper, we introduced SHTC, to our knowledge, the first end-to-end optimized transform coding framework for 3DGS compression, which achieves substantial R-D gains and improved inference efficiency with only minimal parameter overhead. By leveraging learned analysis–synthesis transforms for decorrelation instead of relying solely on highly complex entropy models, SHTC improves compression efficiency and reduces decoding latency, making it well suited to consumer-facing scenarios where fast transmission and decoding are critical. SHTC has the potential to inspire future work on 3DGS compression, for example by motivating more expressive transform architectures and spatially adaptive variants. More broadly, the idea of incorporating signal priors to improve the parameter efficiency of neural codecs may benefit the design of low-complexity neural image and video codecs.

References

[1] Muhammad Salman Ali, Sung-Ho Bae, and Enzo Tartaglione. Elmgs: Enhancing memory and computation scalability through compression for 3d gaussian splatting. *arXiv preprint arXiv:2410.23213*, 2024. 2, 20

[2] Muhammad Salman Ali, Yeongwoong Kim, Maryam Qamar, Sung-Chang Lim, Donghyun Kim, Chaoning Zhang, Sung-Ho Bae, and Hui Yong Kim. Towards efficient image compression without autoregressive models. *Advances in Neural Information Processing Systems*, 36, 2024. 4

[3] Muhammad Salman Ali, Maryam Qamar, Sung-Ho Bae, and Enzo Tartaglione. Trimming the fat: Efficient compression of 3d gaussian splats through pruning. *arXiv preprint arXiv:2406.18214*, 2024. 2, 20

[4] Muhammad Salman Ali, Chaoning Zhang, Marco Cagnazzo, Giuseppe Valenzise, Enzo Tartaglione, and Sung-Ho Bae. Compression in 3d gaussian splatting: A survey of methods, trends, and future directions. *arXiv preprint arXiv:2502.19457*, 2025. 2

[5] Johannes Ballé, Valero Laparra, and Eero P Simoncelli. End-to-end optimized image compression. *arXiv preprint arXiv:1611.01704*, 2016. 4

[6] Johannes Ballé, David Minnen, Saurabh Singh, Sung Jin Hwang, and Nick Johnston. Variational image compression with a scale hyperprior. *arXiv preprint arXiv:1802.01436*, 2018. 1, 2, 4

[7] Jonathan T Barron, Ben Mildenhall, Dor Verbin, Pratul P Srinivasan, and Peter Hedman. Mip-nerf 360: Unbounded anti-aliased neural radiance fields. In *Proceedings of the IEEE/CVF conference on computer vision and pattern recognition*, pages 5470–5479, 2022. 2, 6

[8] Gisle Bjontegaard. Calculation of average psnr differences between rd-curves. *ITU SG16 Doc. VCEG-M33*, 2001. 6

[9] Eric R Chan, Connor Z Lin, Matthew A Chan, Koki Nagano, Boxiao Pan, Shalini De Mello, Orazio Gallo, Leonidas J Guibas, Jonathan Tremblay, Sameh Khamis, et al. Efficient geometry-aware 3d generative adversarial networks. In *Proceedings of the IEEE/CVF conference on computer vision and pattern recognition*, pages 16123–16133, 2022. 21

[10] Anpei Chen, Zexiang Xu, Andreas Geiger, Jingyi Yu, and Hao Su. Tensorf: Tensorial radiance fields. In *European conference on computer vision*, pages 333–350. Springer, 2022. 20

[11] Yihang Chen, Qianyi Wu, Weiyao Lin, Mehrtash Harandi, and Jianfei Cai. Hac: Hash-grid assisted context for 3d gaussian splatting compression. In *European Conference on Computer Vision*, pages 422–438. Springer, 2024. 1, 4, 6, 12, 18

[12] Yihang Chen, Mengyao Li, Qianyi Wu, Weiyao Lin, Mehrtash Harandi, and Jianfei Cai. Pcg: Progressive compression of 3d gaussian splatting. *arXiv preprint arXiv:2503.08511*, 2025. 6

[13] Yihang Chen, Qianyi Wu, Mengyao Li, Weiyao Lin, Mehrtash Harandi, and Jianfei Cai. Fast feedforward 3d gaussian splatting compression. In *The Thirteenth International Conference on Learning Representations*, 2025. 7, 17, 18

[14] Yihang Chen, Qianyi Wu, Weiyao Lin, Mehrtash Harandi, and Jianfei Cai. Hac++: Towards 100x compression of 3d gaussian splatting. *IEEE Transactions on Pattern Analysis and Machine Intelligence*, pages 1–17, 2025. 1, 2, 3, 5, 6, 7, 12, 18

[15] Zhengxue Cheng, Heming Sun, Masaru Takeuchi, and Jiro Katto. Learned image compression with discretized gaussian mixture likelihoods and attention modules. In *Proceedings of the IEEE/CVF conference on computer vision and pattern recognition*, pages 7939–7948, 2020. 1, 4

[16] Ricardo L De Queiroz and Philip A Chou. Compression of 3d point clouds using a region-adaptive hierarchical transform. *IEEE Transactions on Image Processing*, 25(8):3947–3956, 2016. 21

[17] David L Donoho. Compressed sensing. *IEEE Transactions on information theory*, 52(4):1289–1306, 2006. 2, 5

[18] Zhiwen Fan, Kevin Wang, Kairun Wen, Zehao Zhu, Dejia Xu, Zhangyang Wang, et al. Lightgaussian: Unbounded 3d gaussian compression with 15x reduction and 200+ fps. *Advances in neural information processing systems*, 37: 140138–140158, 2024. 2, 7, 17, 18, 20

[19] Sara Fridovich-Keil, Giacomo Meanti, Frederik Rahbæk Warburg, Benjamin Recht, and Angjoo Kanazawa. K-planes: Explicit radiance fields in space, time, and appearance. In *Proceedings of the IEEE/CVF Conference on Computer Vision and Pattern Recognition*, pages 12479–12488, 2023. 20

[20] Sharath Girish, Kamal Gupta, and Abhinav Shrivastava. Eagles: Efficient accelerated 3d gaussians with lightweight encodings. In *European Conference on Computer Vision*, pages 54–71. Springer, 2024. 2, 7, 17, 18, 20

[21] Danillo Graziosi, Ohji Nakagami, Shinroku Kuma, Alexandre Zaghetto, Teruhiko Suzuki, and Ali Tabatabai. An overview of ongoing point cloud compression standardization activities: Video-based (v-pcc) and geometry-based (g-pcc). *APSIPA Transactions on Signal and Information Processing*, 9:e13, 2020. 5

[22] Karol Gregor and Yann LeCun. Learning fast approximations of sparse coding. In *Proceedings of the 27th international conference on international conference on machine learning*, pages 399–406, 2010. 2, 5

[23] Alex Hanson, Allen Tu, Vasu Singla, Mayuka Jayawardhana, Matthias Zwicker, and Tom Goldstein. Pup 3d-gs: Principled uncertainty pruning for 3d gaussian splatting. In *Proceedings of the Computer Vision and Pattern Recognition Conference*, pages 5949–5958, 2025. 2, 7, 17, 18, 20

[24] Dailan He, Ziming Yang, Weikun Peng, Rui Ma, Hongwei Qin, and Yan Wang. Elic: Efficient learned image compression with unevenly grouped space-channel contextual adaptive coding. In *Proceedings of the IEEE/CVF Conference on Computer Vision and Pattern Recognition*, pages 5718–5727, 2022. 4

[25] Peter Hedman, Julien Philip, True Price, Jan-Michael Frahm, George Drettakis, and Gabriel Brostow. Deep blending for free-viewpoint image-based rendering. *ACM Transactions on Graphics (ToG)*, 37(6):1–15, 2018. 2, 6

[26] He Huang, Wenjie Huang, Qi Yang, Yiling Xu, and Zhu Li. A hierarchical compression technique for 3d gaussian

splatting compression. In *ICASSP 2025-2025 IEEE International Conference on Acoustics, Speech and Signal Processing (ICASSP)*, pages 1–5. IEEE, 2025. 21

[27] Bernhard Kerbl, Georgios Kopanas, Thomas Leimkühler, and George Drettakis. 3d gaussian splatting for real-time radiance field rendering. *ACM Trans. Graph.*, 42(4):139–1, 2023. 1, 7, 17, 18

[28] Arno Knapitsch, Jaesik Park, Qian-Yi Zhou, and Vladlen Koltun. Tanks and temples: Benchmarking large-scale scene reconstruction. *ACM Transactions on Graphics (ToG)*, 36(4):1–13, 2017. 2, 6

[29] Joo Chan Lee, Daniel Rho, Xiangyu Sun, Jong Hwan Ko, and Eunbyung Park. Compact 3d gaussian representation for radiance field. In *Proceedings of the IEEE/CVF Conference on Computer Vision and Pattern Recognition*, pages 21719–21728, 2024. 2, 7, 17, 18, 20

[30] Joo Chan Lee, Jong Hwan Ko, and Eunbyung Park. Optimized minimal 3d gaussian splatting. *arXiv preprint arXiv:2503.16924*, 2025. 8, 17

[31] Soonbin Lee, Fangwen Shu, Yago Sanchez, Thomas Schierl, and Cornelius Hellge. Compression of 3d gaussian splatting with optimized feature planes and standard video codecs. *arXiv preprint arXiv:2501.03399*, 2025. 2, 7, 8, 17, 18, 21

[32] Jiahao Li, Bin Li, and Yan Lu. Neural video compression with feature modulation. In *Proceedings of the IEEE/CVF Conference on Computer Vision and Pattern Recognition*, pages 26099–26108, 2024. 1

[33] Sicheng Li, Hao Li, Yiyi Liao, and Lu Yu. Nerfcode: Neural feature compression meets neural radiance fields for memory-efficient scene representation. In *Proceedings of the IEEE/CVF Conference on Computer Vision and Pattern Recognition*, pages 21274–21283, 2024. 20

[34] Jinming Liu, Heming Sun, and Jiro Katto. Learned image compression with mixed transformer-cnn architectures. In *Proceedings of the IEEE/CVF conference on computer vision and pattern recognition*, pages 14388–14397, 2023. 4

[35] Lei Liu, Zhenghao Chen, and Dong Xu. Hemgs: A hybrid entropy model for 3d gaussian splatting data compression. *arXiv preprint arXiv:2411.18473*, 2024. 1, 3, 6

[36] Xiangrui Liu, Xinju Wu, Pingping Zhang, Shiqi Wang, Zhu Li, and Sam Kwong. Compgs: Efficient 3d scene representation via compressed gaussian splatting. In *Proceedings of the 32nd ACM International Conference on Multimedia*, pages 2936–2944, 2024. 7, 17, 18

[37] Tao Lu, Mulin Yu, Linning Xu, Yuanbo Xiangli, Limin Wang, Dahua Lin, and Bo Dai. Scaffold-gs: Structured 3d gaussians for view-adaptive rendering. In *Proceedings of the IEEE/CVF Conference on Computer Vision and Pattern Recognition*, pages 20654–20664, 2024. 1, 2, 8, 17, 18

[38] Jingui Ma, Yang Hu, Luyang Tang, Jiayu Yang, Yongqi Zhai, and Ronggang Wang. Enhancing 3d gaussian splatting compression via spatial condition-based prediction. *arXiv preprint arXiv:2503.23337*, 2025. 7, 17, 18

[39] Ben Mildenhall, Pratul P Srinivasan, Matthew Tancik, Jonathan T Barron, Ravi Ramamoorthi, and Ren Ng. Nerf: Representing scenes as neural radiance fields for view synthesis. *Communications of the ACM*, 65(1):99–106, 2021. 12, 13, 20

[40] David Minnen and Saurabh Singh. Channel-wise autoregressive entropy models for learned image compression. In *2020 IEEE International Conference on Image Processing (ICIP)*, pages 3339–3343. IEEE, 2020. 2

[41] David Minnen, Johannes Ballé, and George D Toderici. Joint autoregressive and hierarchical priors for learned image compression. *Advances in neural information processing systems*, 31, 2018. 1, 4

[42] Wieland Morgenstern, Florian Barthel, Anna Hilsmann, and Peter Eisert. Compact 3d scene representation via self-organizing gaussian grids. In *European Conference on Computer Vision*, pages 18–34. Springer, 2024. 2, 7, 8, 17, 18, 21

[43] Thomas Müller, Alex Evans, Christoph Schied, and Alexander Keller. Instant neural graphics primitives with a multiresolution hash encoding. *ACM transactions on graphics (TOG)*, 41(4):1–15, 2022. 20

[44] KL Navaneet, Kossar Pourahmadi Meibodi, Soroush Abbasi Koohpayegani, and Hamed Pirsiavash. Compgs: Smaller and faster gaussian splatting with vector quantization. In *European Conference on Computer Vision*, pages 330–349. Springer, 2024. 2, 7, 17, 18, 20

[45] Simon Niedermayr, Josef Stumpfegger, and Rüdiger Westermann. Compressed 3d gaussian splatting for accelerated novel view synthesis. In *Proceedings of the IEEE/CVF Conference on Computer Vision and Pattern Recognition*, pages 10349–10358, 2024. 7, 17, 18, 20

[46] Michael Niemeyer, Fabian Manhardt, Marie-Julie Rakotosaona, Michael Oechsle, Daniel Duckworth, Rama Gosula, Keisuke Tateno, John Bates, Dominik Kaeser, and Federico Tombari. Radsplat: Radiance field-informed gaussian splatting for robust real-time rendering with 900+ fps. *arXiv preprint arXiv:2403.13806*, 2024. 2, 20

[47] Panagiotis Papantonakis, Georgios Kopanas, Bernhard Kerbl, Alexandre Lanvin, and George Drettakis. Reducing the memory footprint of 3d gaussian splatting. *Proceedings of the ACM on Computer Graphics and Interactive Techniques*, 7(1):1–17, 2024. 7, 17, 18, 20

[48] Tuan Pham and Stephan Mandt. Neural nerf compression. *arXiv preprint arXiv:2406.08943*, 2024. 20

[49] Daniel Rho, Byeonghyeon Lee, Seungtae Nam, Joo Chan Lee, Jong Hwan Ko, and Eunbyung Park. Masked wavelet representation for compact neural radiance fields. In *Proceedings of the IEEE/CVF Conference on Computer Vision and Pattern Recognition*, pages 20680–20690, 2023. 20

[50] Aliaksei Sandryhaila and José MF Moura. Discrete signal processing on graphs: Graph fourier transform. In *2013 IEEE International Conference on Acoustics, Speech and Signal Processing*, pages 6167–6170. IEEE, 2013. 21

[51] Seungjoo Shin, Jaesik Park, and Sunghyun Cho. Locality-aware gaussian compression for fast and high-quality rendering. In *The Thirteenth International Conference on Learning Representations*, 2025. 7, 17, 18

[52] Cheng Sun, Min Sun, and Hwann-Tzong Chen. Direct voxel grid optimization: Super-fast convergence for radiance fields reconstruction. In *Proceedings of the IEEE/CVF conference on computer vision and pattern recognition*, pages 5459–5469, 2022. 20

[53] Luyang Tang, Yongqi Zhai, Jiayu Yang, Chunhui Yang, and Ronggang Wang. Feature prediction for 3d gaussian splatting compression. In *2025 Data Compression Conference (DCC)*, pages 73–82. IEEE, 2025. 7, 17, 18

[54] Zhenyu Tang, Chaoran Feng, Xinhua Cheng, Wangbo Yu, Junwu Zhang, Yuan Liu, Xiaoxiao Long, Wenping Wang, and Li Yuan. Neuralgs: Bridging neural fields and 3d gaussian splatting for compact 3d representations. *arXiv preprint arXiv:2503.23162*, 2025. 17, 18

[55] Boyuan Tian, Qizhe Gao, Siran Xianyu, Xiaotong Cui, and Minjia Zhang. Flexgaussian: Flexible and cost-effective training-free compression for 3d gaussian splatting. In *Proceedings of the 33rd ACM International Conference on Multimedia*, pages 7287–7296, 2025. 7, 17, 18

[56] Chenjunjie Wang, Shashank N Sridhara, Eduardo Pavéz, Antonio Ortega, and Cheng Chang. Adaptive voxelization for transform coding of 3d gaussian splatting data. *arXiv preprint arXiv:2506.00271*, 2025. 21

[57] Henan Wang, Hanxin Zhu, Tianyu He, Runsen Feng, Jianjun Deng, Jiang Bian, and Zhibo Chen. End-to-end rate-distortion optimized 3d gaussian representation. In *European Conference on Computer Vision*, pages 76–92. Springer, 2024. 2, 7, 17, 18, 20

[58] Yufei Wang, Zhihao Li, Lanqing Guo, Wenhan Yang, Alex Kot, and Bihang Wen. ContextGS : Compact 3d gaussian splatting with anchor level context model. In *The Thirty-eighth Annual Conference on Neural Information Processing Systems*, 2024. 1, 3, 7, 18

[59] Zhou Wang, Alan C Bovik, Hamid R Sheikh, and Eero P Simoncelli. Image quality assessment: from error visibility to structural similarity. *IEEE transactions on image processing*, 13(4):600–612, 2004. 6

[60] Yuanbo Xiangli, Lining Xu, Xingang Pan, Nanxuan Zhao, Anyi Rao, Christian Theobalt, Bo Dai, and Dahua Lin. Bungeenerf: Progressive neural radiance field for extreme multi-scale scene rendering. In *European conference on computer vision*, pages 106–122. Springer, 2022. 12, 13

[61] Shuzhao Xie, Weixiang Zhang, Chen Tang, Yunpeng Bai, Rongwei Lu, Shijia Ge, and Zhi Wang. Mesongs: Post-training compression of 3d gaussians via efficient attribute transformation. In *European Conference on Computer Vision*, pages 434–452. Springer, 2024. 7, 8, 17, 18, 21

[62] Shuzhao Xie, Jiahang Liu, Weixiang Zhang, Shijia Ge, Sicheng Pan, Chen Tang, Yunpeng Bai, Cong Zhang, Xiaoya Fan, and Zhi Wang. Sizegs: Size-aware compression of 3d gaussian splatting via mixed integer programming. In *Proceedings of the 33rd ACM International Conference on Multimedia*, pages 8214–8223, 2025. 7, 17, 18

[63] Qi Yang, Kaifa Yang, Yuke Xing, Yiling Xu, and Zhu Li. A benchmark for gaussian splatting compression and quality assessment study. In *Proceedings of the 6th ACM International Conference on Multimedia in Asia*, pages 1–8, 2024. 21

[64] Qi Yang, Le Yang, Geert Van der Auwera, and Zhu Li. HybridGS: High-efficiency gaussian splatting data compression using dual-channel sparse representation and point cloud encoder. In *Forty-second International Conference on Machine Learning*, 2025. 7, 8, 17

[65] Yu-Ting Zhan, Cheng-Yuan Ho, Hebi Yang, Yi-Hsin Chen, Jui Chiu Chiang, Yu-Lun Liu, and Wen-Hsiao Peng. CAT-3DGS: A context-adaptive triplane approach to rate-distortion-optimized 3DGS compression. In *The Thirteenth International Conference on Learning Representations*, 2025. 1, 2, 3, 7, 12, 19

[66] Jian Zhang and Bernard Ghanem. Ista-net: Interpretable optimization-inspired deep network for image compressive sensing. In *Proceedings of the IEEE conference on computer vision and pattern recognition*, pages 1828–1837, 2018. 2, 5

[67] Jiahui Zhang, Fangneng Zhan, Ling Shao, and Shijian Lu. Sogs: Second-order anchor for advanced 3d gaussian splatting. In *Proceedings of the Computer Vision and Pattern Recognition Conference*, pages 11167–11176, 2025. 2, 17, 18

[68] Kai Zhang, Luc Van Gool, and Radu Timofte. Deep unfolding network for image super-resolution. In *Proceedings of the IEEE/CVF conference on computer vision and pattern recognition*, pages 3217–3226, 2020. 2, 5

[69] Richard Zhang, Phillip Isola, Alexei A Efros, Eli Shechtman, and Oliver Wang. The unreasonable effectiveness of deep features as a perceptual metric. In *Proceedings of the IEEE conference on computer vision and pattern recognition*, pages 586–595, 2018. 6

[70] Yinhao Zhu, Yang Yang, and Taco Cohen. Transformer-based transform coding. In *International Conference on Learning Representations*, 2021. 4

[71] Michael Zibulevsky and Michael Elad. L1-l2 optimization in signal and image processing. *IEEE Signal Processing Magazine*, 27(3):76–88, 2010. 2, 5

[72] Renjie Zou, Chunfeng Song, and Zhaoxiang Zhang. The devil is in the details: Window-based attention for image compression. In *Proceedings of the IEEE/CVF conference on computer vision and pattern recognition*, pages 17492–17501, 2022. 4

Learning Hierarchical Sparse Transform Coding of 3DGS

Supplementary Material

7. Overview of the Supplementary Material

This supplementary document provides additional technical details, extended experiments, and ablation studies that complement the main paper. Its content is organized as follows:

- Sec. 8 compares our method with representative anchor-based methods on two additional datasets, **Synthetic-NeRF** [39] and **BungeeNeRF** [60].
- Sec. 9 presents additional comparisons of computational cost between our approach and CAT-3DGS.
- Sec. 10 shows **visual comparisons**.
- Sec. 11 presents more detailed **ablation studies**.
- Sec. 12 provides a more detailed discussion of our **transform choices**.
- Sec. 13 presents additional comparisons in the training time.
- Sec. 14 provides further comparisons with a set of widely used baselines and recent methods.
- Sec. 15 summarizes implementation details.
 - Sec. 15.1 explains how we compute pixel-wise distortion in the YCbCr color space.
 - Sec. 15.2 details the selection of the λ values used to generate the R-D curves in the main paper.
- Sec. 16 discusses the limitations of our approach and outlines directions for future work.
- Sec. 17 reviews additional related work to further contextualize our method.

8. Additional Results on the Synthetic-NeRF and BungeeNeRF Datasets

Fig. 5 compares the R-D curves of our method with several anchor-based 3DGS compression methods on the Synthetic-NeRF [39] and BungeeNeRF [60] datasets. As shown in the figure, our method consistently achieves better R-D performance, attaining a smaller memory footprint at comparable PSNR levels. Tab. 3 further reports the BD-rate gains of our method over three anchor-based baselines. Taken together, these additional experimental results further demonstrate the effectiveness of our approach and serve as a supplementary comparison to the experiments reported in the main text.

9. Additional Comparisons with CAT-3DGS

As a supplement to Table 2 in the main paper, Tab. 4 compares our method with CAT-3DGS. The evaluation metrics include encoding time, decoding time, and BD-rate relative to the HAC baseline. With HAC as the common baseline,

Dataset	HAC++	CAT-3DGS (40k)	HAC
Synthetic-NeRF	-13.45%	-	-26.33%
BungeeNeRF	-10.04%	-39.90%	-52.05%

Table 3. The BD-rate of our method relative to three baselines: HAC++ [14], CAT-3DGS [65] and HAC [11]. Negative values indicate bitrate savings (better) compared with each baseline.

	Encoding time (s)↓		Decoding time (s)↓		BD-rate↓	
	CAT-3DGS	Ours	CAT-3DGS	Ours	CAT-3DGS	Ours
Mip-NeRF360	79.82	5.90	87.95	8.86	-53.48%	-64.82%
Tank&Temples	34.95	3.91	38.11	5.80	-45.99%	-56.06%
DeepBlending	15.60	2.30	18.99	3.18	-52.62%	-64.56%

Table 4. Evaluating the effectiveness: CAT-3DGS vs. SHTC + simple entropy model. From left to right, we report four metrics: encoding time, decoding time, and BD-rate relative to the HAC baseline. The best result for each metric is highlighted in **bold**.

our method achieves a larger reduction in memory footprint while requiring substantially less encoding and decoding time at inference. For CAT-3DGS [65], we encountered out-of-memory (OOM) errors during rendering when running the official implementation on our hardware, so the rendering FPS could not be measured. However, the training time, encoding time, and decoding time can still be measured before this OOM issue occurs. Consequently, we omit the rendering-FPS comparison for CAT-3DGS in the table.

10. Visual Comparison

We provide visual comparisons between our SHTC approach and HAC++ [14] in Fig. 6. For each example, we report the bitstream size (in MB) and the PSNR (in dB) of the shown crop. To illustrate how SHTC reduces rendering distortion under a smaller or comparable memory footprint, we evaluate four representative scenes: ‘playroom’ (DeepBlending), ‘train’ (Tanks & Temples), and ‘garden’ and ‘stump’ (Mip-NeRF360), which are shown from the first to the fourth row in Fig. 6. In the ‘playroom’ scene, our method better preserves the structure of the wall-mounted switch, which appears as an unrecognizable blur in the HAC++ reconstruction. In the ‘train’ scene, our method suppresses shading and dark banding artifacts along the painted stripes. In the ‘garden’ scene, our method removes the black floater near the table edge. In the ‘stump’ scene, our method effectively reduces floater artifacts around the tree stump.

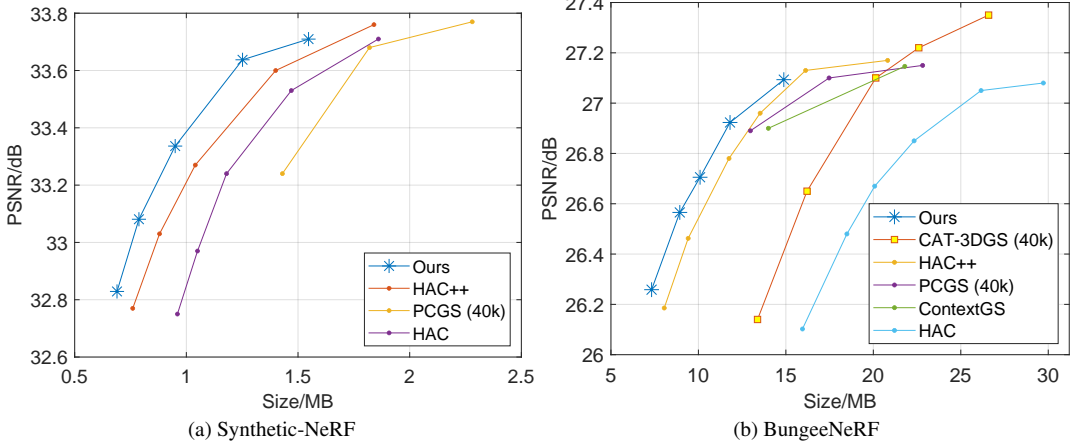


Figure 5. Comparison of our method with anchor-based methods on two additional datasets, Synthetic-NeRF [39] and BungeeNeRF [60].

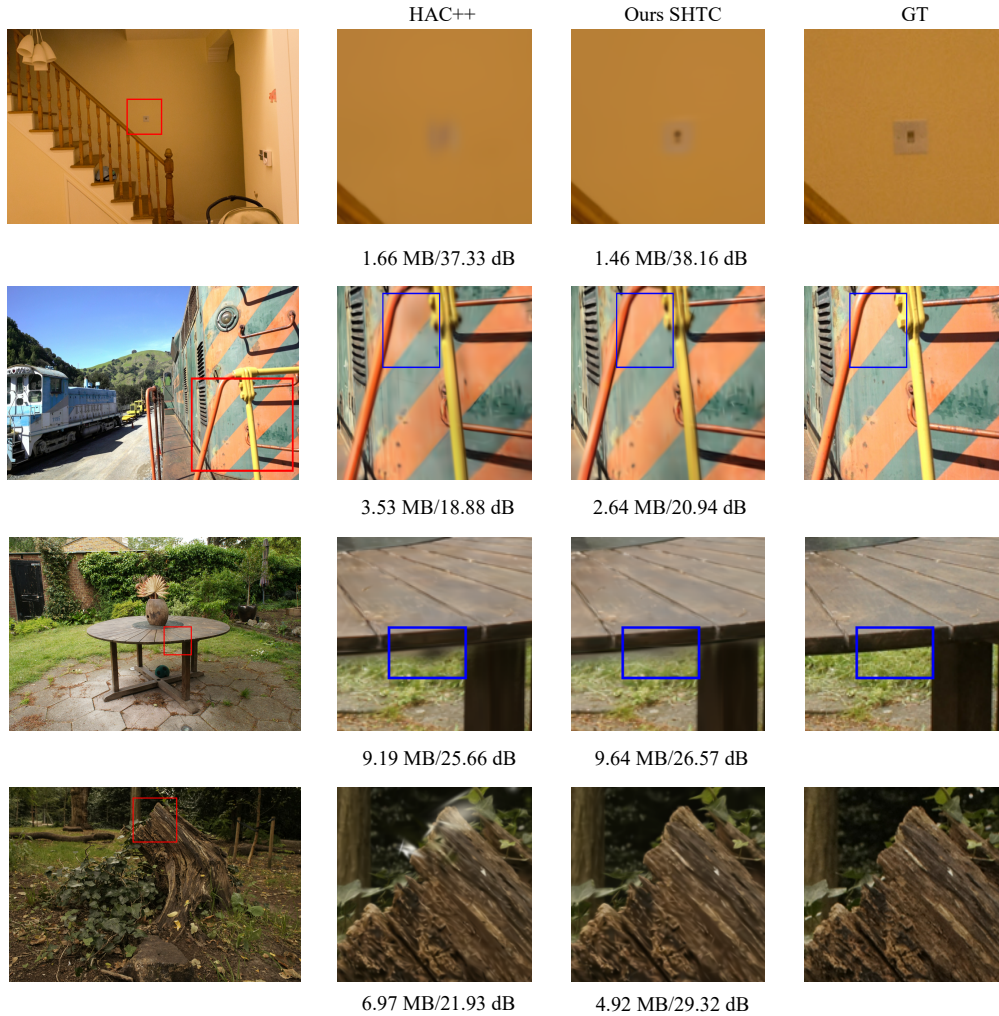


Figure 6. Visual comparison between HAC++ and our SHTC method on four scenes: ‘playroom’ (DeepBlending), ‘train’ (Tanks & Temples), ‘garden’ and ‘stump’ (Mip-NeRF360).

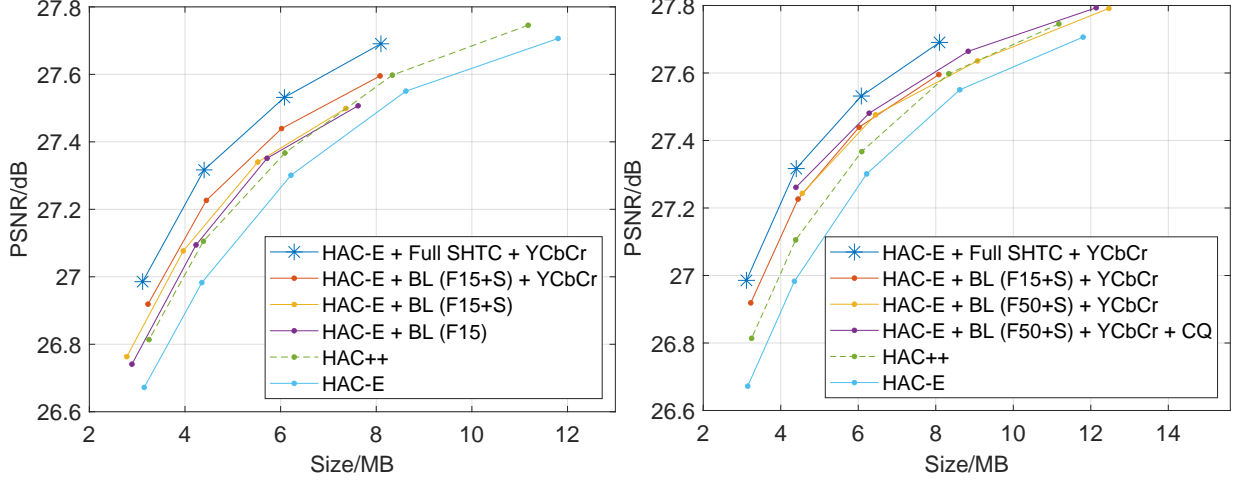


Figure 7. Ablation Study of SHTC Variants on Mip-NeRF360.

11. Additional Ablation Study

11.1. Additional Quantitative Ablation Study

In the main paper, we only report the most basic configuration and the complete version of our method, mainly to let readers grasp the overall benefit of SHTC at a glance under the page limit. In this subsection, we present a more fine-grained quantitative ablation study to isolate and measure the contribution of each component that bridges the basic configuration and the full model.

To more accurately quantify the gains brought by the proposed transform modules, we construct an enhanced version of HAC, denoted by **HAC-E**. HAC-E is an intermediate variant between the vanilla HAC and HAC++. Following HAC++, HAC-E uses MPEG-GPCC to compress anchor positions and adopts the mask-aware rate estimator, but it still retains the simple entropy model of HAC and does not use complex context modeling. Starting from this common baseline, there are two ways to further improve compression performance:

1. replacing the simple entropy model with a highly complex one, which leads to HAC++;
2. keeping the simple, fast entropy model while introducing learned transforms to enhance R-D performance, which is our transform-coding paradigm.

Along the second route, we build several SHTC variants on top of HAC-E, and their BD-rate values over HAC-E directly quantify the gains of each component. Starting from HAC-E, we progressively add components:

- **HAC-E + BL(F15)**: we activate the most basic version of SHTC and use only its base layer (BL), implemented as a KLT, to compress anchor features. The dimensionality of

the principal coefficients is set to 15.

- **HAC-E + BL(F15+S)**: we use the base layer to compress both anchor features and anchor scalings, as described in the main text.
- **HAC-E + BL(F15+S) + YCbCr**: building on the previous variant, we replace the original pixel-wise ℓ_1 distortion with the proposed YCbCr-space distortion \mathcal{L}_{YCbCr} in the training objective.
- **HAC-E + Full SHTC + YCbCr**: finally, we use the full two-layer SHTC for anchor feature compression, so that the neural refinement layer compensates for truncation loss at low rate overhead, while the base layer is still used for anchor scaling compression. This corresponds to our full model.

We plot the R-D curves of these variants on the Mip-NeRF360 dataset in Fig. 7a. Mip-NeRF360 contains diverse and challenging indoor and outdoor scenes, making it a suitable benchmark for ablation with reduced bias. From Fig. 7a, we observe that introducing a KLT-based base layer for anchor feature compression (HAC-E + BL(F15)) already yields a clear gain over the HAC-E baseline and brings the performance close to HAC++. Extending the base layer to also compress anchor scalings (HAC-E + BL(F15+S)) and further switching to the YCbCr-based distortion metric (HAC-E + BL(F15+S) + YCbCr) provide additional, consistent improvements. The complete SHTC configuration trained with the YCbCr-based distortion (HAC-E + Full SHTC + YCbCr) achieves the best overall R-D trade-off among all variants.

Tab. 5 quantifies these effects by reporting BD-rate values over HAC-E on Mip-NeRF360. HAC++ is also included to facilitate a direct comparison between the two

paradigms: using learned transforms with a simple entropy model versus relying solely on a highly complex entropy model. The results show that even the simplest transform-based variant (HAC-E + BL(F15)) already surpasses HAC++, and each additional component yields further BD-rate reductions, leading to a substantial 29.33% reduction for HAC-E + Full SHTC + YCbCr.

BD-rate over HAC-E	
HAC++	-10.93%
HAC-E+BL(F15)	-13.30%
HAC-E+BL(F15+S)	-16.59%
HAC-E+BL(F15+S)+YCbCr	-20.07%
HAC-E+Full SHTC+YCbCr	-29.33%

Table 5. BD-rate over HAC-E on the Mip-NeRF360 dataset for HAC++ and the proposed SHTC variants. Negative values indicate rate savings over HAC-E, and more negative values correspond to better R-D performance.

11.2. Comparison with No-Truncation Variants

Finally, we investigate whether directly transmitting all KLT coefficients can serve as a competitive alternative to our truncated-plus-refinement design. In Fig. 7b, we first consider a variant that does *not* truncate the KLT coefficients of anchor features, denoted by HAC-E + BL(F50+S) + YCbCr. This configuration directly quantizes and entropy-codes all 50 KLT coefficients. Under the same rate-control parameter λ , it attains higher PSNR than the truncated-only baseline, but at a significantly higher bitrate, so it offers no improvement in overall R-D performance compared with simply truncating the coefficients.

Building on HAC-E + BL(F50+S) + YCbCr, we then introduce a monotonically increasing, channel-wise quantization schedule for the 50-dimensional KLT coefficients,

$$q_s^{(i)} = q_s \exp(\alpha i), \quad i \in \{0, \dots, 49\}, \quad (10)$$

where α is a learnable scalar and q_s is the per-anchor base quantization step predicted by HAC. The idea is to reduce the bitrate cost of transmitting all coefficients by assigning larger quantization steps to less important channels. This variant, denoted by HAC-E + BL(F50+S) + YCbCr + CQ, yields a modest improvement over HAC-E + BL(F50+S) + YCbCr, but still falls short of our truncated-plus-refinement scheme in terms of R-D performance.

These results confirm that directly transmitting all KLT coefficients, even with a more sophisticated quantization schedule, is rate-inefficient and does not bring meaningful gains in R-D performance. In contrast, truncating the transform coefficients and compensating the lost information via a learned refinement layer provides a more effective and bitrate-efficient way to improve compression performance.

12. Discussion of Transform Choices

12.1. Transform Choices for the Base Layer

In this section, we present a high-level comparison of transform design choices, supported by several analysis experiments.

Why Not DCT or DWT? We considered several candidates for the base-layer transform, including the classical DCT and the Haar wavelet. To guide this choice, we compared their ability to decorrelate anchor channels and compact energy. Fig. 8 shows the absolute inter-channel correlation matrices and the normalized energy distributions of the original HAC features, the DCT coefficients, the Haar coefficients, and the KLT coefficients. DCT and Haar can reduce inter-channel correlation and slightly improve energy compactness, but their gains are limited: the correlation matrices still exhibit noticeable off-diagonal structure and the energy remains relatively spread out across channels. This behavior is expected because their bases are fixed and data-agnostic. In contrast, KLT yields an almost perfectly diagonal correlation matrix and concentrates most of the energy in the first few coefficients. This data-dependent transform is obtained as the eigenvectors of the sample covariance and is theoretically optimal for decorrelation and energy compaction among linear transforms. The main additional cost, relative to DCT and Haar, is storing the KLT basis. Even if the full basis must be transmitted, a 50-dimensional feature vector only requires a 50×50 matrix (2,500 coefficients), which is negligible compared with the overall bitstream size.

Why Not an MLP-Based Transform? Beyond classical transforms, we also compare our ‘HAC-E + KLT (F15)’ variant (the simplest version of SHTC) with a variant equipped with an MLP-based analysis and synthesis transform pair. Both networks are 5-layer MLPs, with a total of 21,930 parameters that must be transmitted as part of the bitstream. This comparison, evaluated on the Mip-NeRF360 dataset and shown in Fig. 9, reveals that the black-box MLP transform performs significantly worse in terms of the R-D trade-off than the simple KLT-based design. A likely reason is that, under a strict parameter budget, the MLP-based transform lacks sufficient expressive power to accurately reconstruct the input, leading to larger reconstruction errors and thus worse R-D performance.

For these reasons, we adopt KLT as a cost-effective choice for the base-layer transform. KLT provides strong decorrelation and energy compaction at negligible storage cost, while remaining simple and invertible. On top of this, we use a neural residual coder to compensate for the truncation loss of the KLT coefficients, which further improves the R-D performance over using KLT alone.

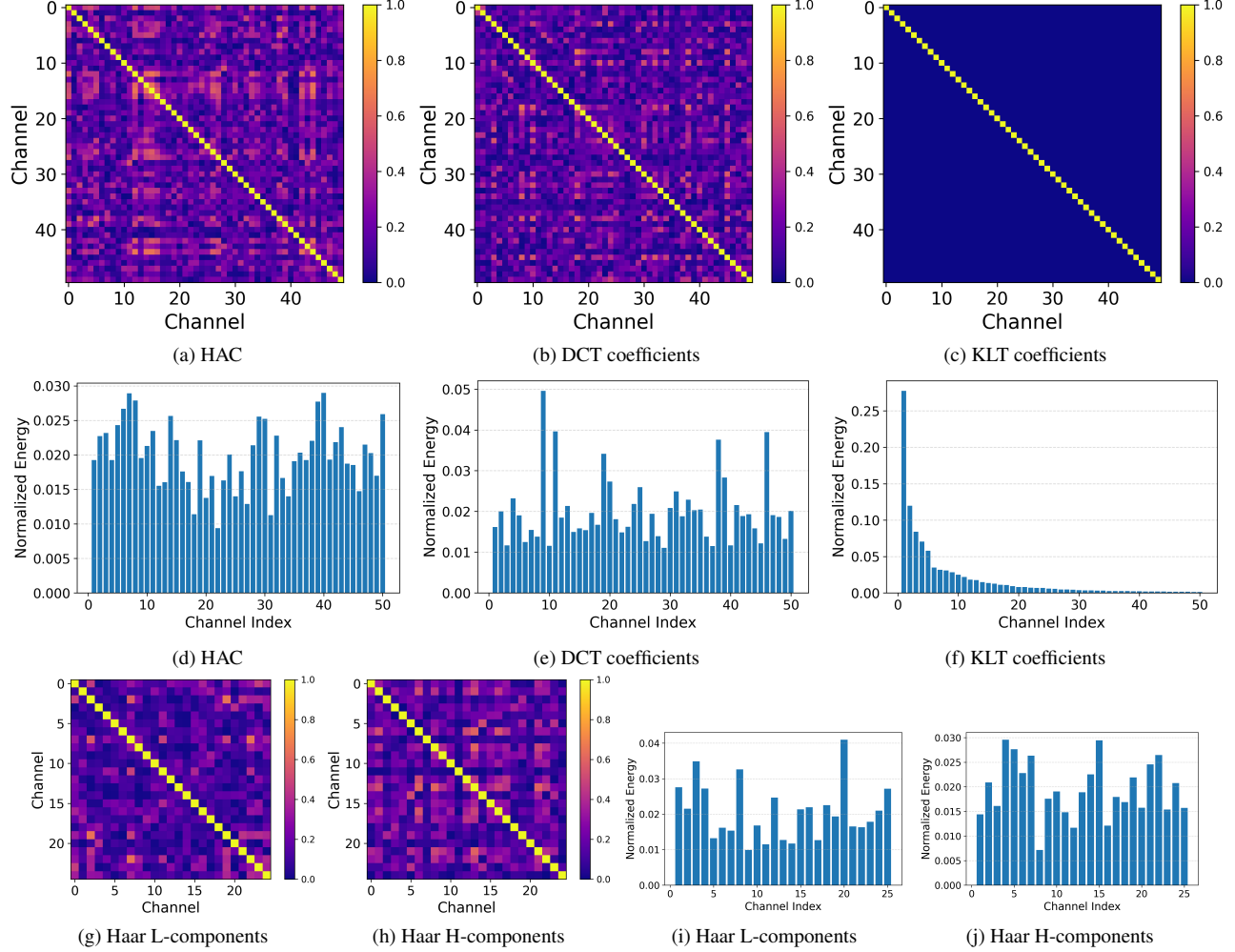


Figure 8. Inter-channel decorrelation and energy compaction across transforms. (a-c) Absolute inter-channel correlation matrices for the original data, DCT coefficients, and KLT coefficients. (d-f) Normalized energy per channel. (g-h) Absolute inter-channel correlation for the Haar transform’s two sub-bands. (i-j) Corresponding normalized energy distributions for Haar L and Haar H sub-bands.

12.2. Transform Choices for the Refinement Layer

When designing the neural refinement layer, a natural question arises: why not simply use a generic MLP? Our key observation is that the residual to be coded by the refinement layer (i.e., the KLT residual) can be reasonably modeled as a sparse signal. Classical compressed sensing theory shows that sparse signals can be recovered from a small number of linear measurements by solving a sparsity-regularized inverse problem. This perspective suggests a principled way to construct the refinement layer: instead of relying on an unconstrained black-box network, we explicitly exploit sparsity and build the module on top of a well-understood sparse reconstruction framework, so that each component has a clear interpretation.

In 3DGS compression, the parameters of transforms must be transmitted as part of the bitstream, so the parame-

ter budget is limited. Under such constraints, a purely neural, black-box MLP may not have sufficient effective capacity to learn a good transform and its approximate inverse from data. In contrast, a sparsity-aware design embeds strong structure and prior knowledge directly into the architecture, so that even with relatively few parameters it can still achieve accurate reconstruction. This leads to much higher parameter efficiency than a generic MLP-based transform.

To verify this intuition, we conduct several offline experiments; here we present results on the *bicycle* scene of the Mip-NeRF360 dataset, where we compress the KLT residual in two different ways. The first variant uses a pure MLP-based transform with an MLP analysis and synthesis transform pair; both networks are 5-layer MLPs, resulting in a total of 21,930 parameters that must be transmitted in the

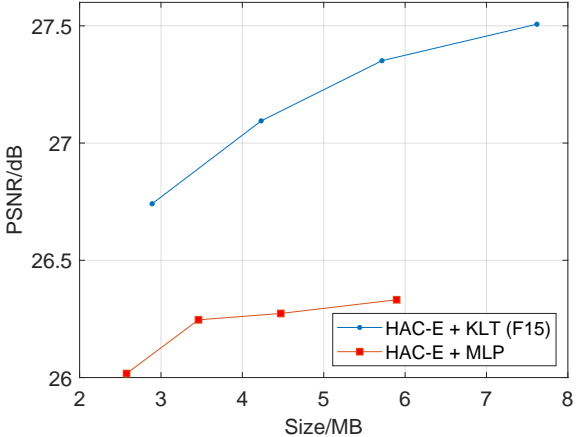


Figure 9. Comparison between ‘HAC-E + KLT (F15)’ and ‘HAC-E + MLP’ on the Mip-NeRF360 dataset.

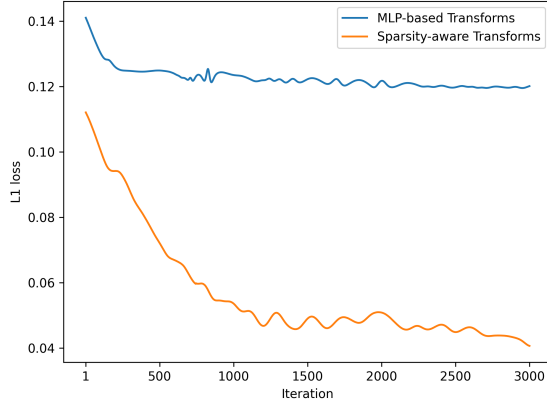


Figure 10. Offline comparison of our sparsity-aware refinement layer and a black-box MLP-based transform on the *bicycle* scene of the Mip-NeRF360 dataset. The plot shows the ℓ_1 reconstruction loss of the KLT residual versus training iteration.

bitstream. The second variant uses our sparsity-aware refinement layer, which contains only 5,093 parameters. We train both models for 3,000 iterations and measure the ℓ_1 reconstruction loss of the KLT residual. As shown in Fig. 10, the sparsity-aware transform consistently drives the loss down to a much lower level than the MLP-based transform, despite using roughly four times fewer parameters. This early-stage verification supports our motivation: leveraging the sparsity prior and using a compressed-sensing-inspired architecture for residual coding yields a highly parameter-efficient refinement module. For this reason, we adopt the sparsity-aware design as our default choice for the neural refinement layer in SHTC.

13. Training time

Tab. 6 compares the training time of our method with three advanced anchor-based 3DGS compression methods that rely on complex entropy models. Although our method is not the fastest to train, its training time remains moderate: it requires more training time than HAC++, but consistently less than CAT-3DGS and ContextGS across all three benchmarks. Designing a compression system that simultaneously attains the best possible training efficiency, R-D performance, and inference speed is notoriously difficult; in practice, there is no free lunch. We argue that the resulting overhead in training time is acceptable because 3DGS compression follows a “compress once, decompress many times” paradigm. Training is a one-time offline cost borne by 3DGS asset producers, whereas decoding is performed repeatedly on the user side. End users are therefore insensitive to training time but directly affected by download and decoding latency. In this context, trading a modest increase in training time for improved R-D performance and faster decoding is both realistic and, in practice, a favorable design choice. Our method realizes this trade-off in practice, achieving improved R-D performance and lower decoding latency while keeping the training time within a reasonable range.

	CAT-3DGS	ContextGS	HAC++	Ours
Mip-NeRF360	5725	3927	2735	3218
Tank&Temples	4034	2505	1880	2315
DeepBlending	3353	2320	1857	2270

Table 6. Training time (in seconds) of CAT-3DGS, ContextGS, HAC++, and our method on three datasets. The best and second-best results are highlighted in red and yellow cells, respectively.

14. Additional Comparisons with Other Methods

In addition to the comparisons with anchor-based compression methods using R-D curves and BD-rate, we also evaluate our method against a broad set of anchor-free and hybrid baselines. These include several commonly used 3DGS and compression baselines [18, 20, 27, 29, 36, 37, 42, 44, 45, 47, 57], the feed-forward compression method FCGS [13], and two neural-field-based 3DGS compression methods, LocoGS [51] and NeuralGS [54]. We further consider several recent 3DGS compression methods [23, 30, 55, 62], two HAC-based approaches that introduce prediction modules to improve HAC [38, 53], and a group of methods that apply transform coding in a post-training stage for 3DGS compression [31, 42, 61, 64].

Regarding SOGS [67], we do not include it in our quantitative comparison for two reasons. First, to the best of

Datasets	Mip-NeRF360				Tank&Temples				DeepBlending			
Methods	psnr↑	ssim↑	lpips↓	size↓	psnr↑	ssim↑	lpips↓	size↓	psnr↑	ssim↑	lpips↓	size↓
3DGS [27]	27.46	0.812	0.222	750.9	23.69	0.844	0.178	431.0	29.42	0.899	0.247	663.9
Scaffold-GS [37]	27.50	0.806	0.252	253.9	23.96	0.853	0.177	86.50	30.21	0.906	0.254	66.00
Compact3DGS [29]	27.08	0.798	0.247	48.80	23.32	0.831	0.201	39.43	29.79	0.901	0.258	43.21
Compressed3D [45]	26.98	0.801	0.238	28.80	23.32	0.832	0.194	17.28	29.38	0.898	0.253	25.30
EAGLES [20]	27.14	0.809	0.231	58.91	23.28	0.835	0.203	28.99	29.72	0.906	0.249	52.34
LightGaussian [18]	27.00	0.799	0.249	44.54	22.83	0.822	0.242	22.43	27.01	0.872	0.308	33.94
Navaneet <i>et al.</i> [44]	27.12	0.806	0.240	19.33	23.44	0.838	0.198	12.50	29.90	0.907	0.251	13.50
Reduced3DGS [47]	27.19	0.807	0.230	29.54	23.57	0.840	0.188	14.00	29.63	0.902	0.249	18.00
RDOGaussian [57]	27.05	0.802	0.239	23.46	23.34	0.835	0.195	12.03	29.63	0.902	0.252	18.00
PUP 3D-GS [23]	26.67	0.786	0.272	74.65	22.72	0.801	0.244	43.33	28.85	0.881	0.302	69.92
SizeGS [62]	27.48	0.806	0.240	18.17	24.04	0.840	0.200	10.93	30.24	0.903	0.271	7.92
FlexGaussian [55]	26.38	0.780	0.251	40.80	22.44	0.804	0.219	16.30	28.61	0.884	0.269	25.48
NeuralGS [54]	27.35	0.806	0.240	16.90	23.63	0.841	0.192	12.06	29.91	0.906	0.254	12.98
LocoGS [51]	27.40	0.815	0.219	13.89	23.89	0.854	0.160	12.34	30.17	0.906	0.244	13.39
FCGS (low rate) [13]	27.05	0.798	0.237	36.30	23.48	0.833	0.193	18.80	29.27	0.893	0.257	30.10
FCGS (high rate) [13]	27.39	0.806	0.226	67.20	23.62	0.839	0.184	33.60	29.58	0.899	0.248	54.50
SOG [42]	26.56	0.791	0.241	16.70	23.15	0.828	0.198	9.30	29.12	0.892	0.270	5.70
CodecGS [31]	27.30	0.810	0.236	9.78	23.63	0.842	0.192	7.46	29.82	0.907	0.251	8.62
MesonGS [61]	26.99	0.796	0.247	27.16	23.32	0.837	0.193	16.99	29.51	0.901	0.251	24.76
CompGS [36]	27.26	0.803	0.239	16.50	23.70	0.837	0.208	9.60	29.69	0.901	0.279	8.77
FP-Net [38]	27.46	0.801	0.249	11.08	24.13	0.847	0.192	6.34	30.14	0.906	0.274	3.46
FP-GS [53]	27.53	0.806	0.240	12.82	24.32	0.811	0.185	7.32	30.05	0.906	0.266	3.91
HAC [11]	27.53	0.807	0.238	15.26	24.04	0.846	0.187	8.10	29.98	0.902	0.269	4.35
Context-GS [58]	27.62	0.808	0.237	12.68	24.20	0.852	0.184	7.05	30.11	0.907	0.258	3.45
HAC++ [14]	27.60	0.803	0.253	8.34	24.22	0.849	0.190	5.18	30.16	0.907	0.266	2.91
Ours	27.69	0.804	0.248	8.10	24.34	0.845	0.191	5.19	30.19	0.903	0.272	2.49

Table 7. Comparison of our SHTC framework with other 3DGS data compression methods, including 3DGS and Scaffold-GS, for reference. The best and second-best results are highlighted in red and yellow cells, respectively. The size values are measured in megabytes (MB).

our knowledge, there is no official implementation available, and the original paper does not report file sizes or distortion metrics on the datasets used in our experiments, which makes a fair and reproducible comparison difficult. Second, SOGS is essentially a 3DGS compaction method rather than a full compression scheme with an explicit bit-stream and entropy coding. Based on the model statistics reported in [67], we can only roughly infer an effective compression ratio of about $2\times$ over Scaffold-GS; this is merely a rough estimate, since the authors do not provide explicit compression ratios. In contrast, by employing the proposed

SHTC framework, our method achieves substantially higher compression ratios over Scaffold-GS. For these reasons, we omit SOGS from the quantitative comparison.

Because many of the above methods report only one or two operating points on the R-D curve, a meaningful BD-rate computation is not feasible. For these methods, we therefore provide a numerical comparison in tabular form in Tab. 7. As shown in Tab. 7, our method achieves a better memory-quality trade-off than above approaches.

	HAC	ContextGS	HAC++	Ours
Mip-NeRF360	{0.002, 0.004, 0.008, 0.015}	{0.002, 0.004, 0.008, 0.015, 0.025}	{0.002, 0.004, 0.008, 0.015, 0.025}	{0.002, 0.004, 0.008, 0.015}
Tank&Temples	{0.002, 0.004, 0.008, 0.015, 0.025}	{0.002, 0.004, 0.008, 0.015, 0.025, 0.04}	{0.002, 0.004, 0.008, 0.015, 0.025}	{0.002, 0.004, 0.008, 0.015}
DeepBlending	{0.002, 0.004, 0.008, 0.015, 0.025}	{0.002, 0.004, 0.008, 0.015, 0.025, 0.04}	{0.002, 0.004, 0.008, 0.015, 0.025, 0.04}	{0.002, 0.004, 0.008, 0.015, 0.02, 0.025}
Synthetic-NeRF	{0.0005, 0.001, 0.002, 0.003, 0.004}	-	{0.0005, 0.001, 0.002, 0.003, 0.004}	{0.0005, 0.001, 0.002, 0.003, 0.004}
BungeeNeRF	{0.001, 0.002, 0.003, 0.004, 0.006}	{0.001, 0.004}	{0.0005, 0.001, 0.002, 0.003, 0.004, 0.006, 0.008}	{0.001, 0.002, 0.003, 0.004, 0.006}

Table 8. Summary of λ values used to generate R-D curves on different datasets.

15. Implementation Details

15.1. Pixel-wise Error in YCbCr Color Space

We propose a new distortion term for supervising the rendered images, inspired by the YCbCr color transform used in traditional image and video codecs. Because humans are more sensitive to luminance variations than to chrominance, we compute pixel-wise ℓ_1 loss in the YCbCr space and place a higher weight on the Y component. To preserve fine detail, we add a high-frequency fidelity term on the Y channel by encouraging small differences between the Laplacian-filter response maps of I_Y and \hat{I}_Y . To suppress color noise and artifacts, we further impose a total variation (TV) regularizer on the Cb and Cr channels. Together, the distortion term is defined as

$$\begin{aligned} \mathcal{L}_{\text{YCbCr}} = & \ell_1(I_Y, \hat{I}_Y) + \lambda_c \ell_1(I_{Cb}, \hat{I}_{Cb}) + \lambda_c \ell_1(I_{Cr}, \hat{I}_{Cr}) \\ & + \lambda_H \ell_1(\nabla^2 I_Y, \nabla^2 \hat{I}_Y) \\ & + \lambda_{TV} \text{TV}(\hat{I}_{Cb}) + \lambda_{TV} \text{TV}(\hat{I}_{Cr}). \end{aligned} \quad (11)$$

This distortion term acts as a regularizer on the compressed 3DGS representation, encouraging it to render images with reduced luminance errors at a given bitrate, since luminance errors are perceptually more important than chrominance errors. This, in turn, reduces the overall distortion and empirically improves the R-D performance. In our implementation, we set λ_c , λ_H , and λ_{TV} to 0.6, 0.15, and 0.1, respectively.

15.2. Details of λ Selection for R-D Curves

In this subsection, we summarize in Tab. 8 the λ values used to generate the R-D curves in our experiments. In addition to these values, we also clarify several special cases regarding how λ and the corresponding R-D points are obtained for some baselines:

- **Main text.** For the R-D curves in the main paper, we train the model with $\lambda \in \{0.002, 0.004, 0.008, 0.015\}$, which yields a PSNR range of roughly 1 dB. The spacing between consecutive λ value is gradually increased so as to cover a wide bitrate range while providing approximately uniform sampling of the R-D curves within that range. Because different models and datasets exhibit different sensitivity to λ , we additionally use larger λ values for some baselines so that the PSNR range of each curve is comparable to that of the others.

- **CAT-3DGS.** For CAT-3DGS [65], we encountered out-of-memory (OOM) errors during rendering when using the official implementation on our hardware. Consequently, we do not re-train or re-evaluate this method; instead, we directly use the R-D points reported in the original paper as its results in our plots.
- **Synthetic-NeRF.** For experiments on the Synthetic-NeRF dataset, in order to obtain a quick verification of our method under comparable settings, we follow the λ configurations recommended in the original HAC and HAC++. For the HAC, HAC++, and ContextGS baselines, we directly adopt the R-D numbers reported by their authors. Our own method is evaluated by running our implementation with the same λ values.
- **BungeeNeRF.** On the BungeeNeRF dataset, we again start from the λ settings used in the original HAC, HAC++, and ContextGS papers for all methods, including ours. For these baselines, we use the R-D results reported by the authors at their original operating points. In addition, to obtain a PSNR range that is comparable to that of CAT-3DGS for a more reliable BD-rate computation, we further evaluate our method as well as HAC and HAC++ with one or two larger λ values, thereby extending the PSNR variation range of these methods on BungeeNeRF.
- **PCGS.** For PCGS, on both Synthetic-NeRF and BungeeNeRF, we found it difficult to obtain a sufficiently wide PSNR range for a stable BD-rate estimation by tuning λ . Therefore, we only plot the R-D points reported in the original paper and treat PCGS as a qualitative reference rather than including it in the quantitative BD-rate comparison.

16. Limitation and Future Work

In this work, SHTC adopts transforms that is shared across all spatial regions. This global sharing keeps the parameter count and bitstream overhead small and already yields strong R-D gains over existing methods, but it also limits the ability of the transform to adapt to local statistics. A natural extension to further improve performance is to introduce limited spatial adaptivity. For example, one could partition the anchors into blocks and learn a compact bank of transforms, transmitting a few index bits to select the best transform for a given anchor or block, analogous to intra prediction mode selection in video codecs. Since SHTC

is highly parameter-efficient, the additional memory footprint of such a transform bank and the overhead of signaling the transform index would remain modest. As our primary goal in this work is to demonstrate the necessity and effectiveness of incorporating transform coding into the 3DGS training process, we leave the design and evaluation of these spatially adaptive variants for future work.

17. Supplementary Related Work

17.1. Unstructured 3DGS compression methods

3DGS has recently emerged as a pioneering approach for 3D reconstruction and representation, offering both high-quality and real-time rendering. Specifically, it represents a 3D scene as a collection of Gaussian primitives. Each Gaussian is parameterized by a position vector and a covariance matrix, which together define its position, shape and orientation in 3D space. Additionally, each Gaussian is associated with an opacity parameter and a set of Spherical Harmonics (SH) coefficients to model view-dependent colors. Through differentiable rendering techniques, all attributes of the Gaussians can be optimized, and the number of Gaussians can be progressively increased to minimize rendering distortion. However, the unconstrained Gaussian clone/splitting operation can generate millions of Gaussians, leading to the substantial burden on storage and bandwidth. This motivates researchers to explore 3DGS compression. Three observations motivate compressing 3D Gaussian Splatting (3DGS): (i) many Gaussians have negligible impact on rendering quality; (ii) many attributes tolerate reduced numerical precision; and (iii) only a subset of regions require high-order SH coefficients for sharp view-dependent effects. Taken together, these enable effective compression via pruning, SH distillation, and quantization.

Pruning The densification process of 3DGS results in an explosion in the number of Gaussians. While this allows for the reconstruction of finer scene details, a substantial portion of the Gaussians is redundant, and removing them has little effect on visual quality. The challenge lies in identifying these unimportant Gaussians. [44] simply uses opacity as a criterion to remove transparent or nearly invisible Gaussians. [1, 3] further use both gradient magnitude and opacity levels as reference to identify removable Gaussians. Several subsequent studies assess each Gaussian’s contribution to ray color prediction and utilize this as the importance score [18, 20, 46]. Lee *et al.* learn a binary mask to prune those unimportant Gaussians [29], which is adopted by several subsequent works [57]. [23] propose a principled sensitivity pruning score by computing a second-order approximation of the reconstruction error with respect to the parameters of each Gaussian.

SH distillation The largest portion of the memory footprint is used to store SH coefficients for modeling view-dependent color. However, a large fraction of the region consists of diffuse materials, which can be effectively modeled with view-independent color. This leads to significant waste in using high-degree SHs. To address this, [47] assign each Gaussian an appropriate SH degree to reduce waste, while [18] distill knowledge from a high-degree SH teacher model to a student model with truncated, lower-degree SHs.

Scalar quantization Gaussian attributes are typically stored at 32-bit precision. However, opacity, scale, rotation, and SH coefficients are tolerant to small inaccuracies, suggesting that lower bit-depths can represent them with minimal performance drop. In light of this, [47] propose a scalar quantization scheme that assigns each full-precision value to its nearest codeword in a K-means-derived codebook, storing only the corresponding index. [20] learn a latent representation, quantize it using a uniform scalar quantizer, and employ a decoder to predict Gaussian attributes from the quantized representation.

Vector quantization Many Gaussians share similar parameters, allowing similar vectors to be mapped to a common code vector in a codebook. Instead of storing high-precision vectors, only compact indices are needed. Based on this insight, several works apply vector quantization to eliminate the redundancy within Gaussian attributes [18, 44, 45]. Furthermore, [57] employ entropy-constrained vector quantization, incorporating entropy coding into the quantization process. It assigns shorter codes to those code vectors that are used more frequently, effectively compressing the index stream.

17.2. Transform coding in NeRF/3DGS compression

Before the emergence of 3DGS, grid-based NeRF representations [10, 19, 43, 52] were considered a promising alternative to the classic NeRF [39]. Several works have explored the use of transform coding to compress the feature grids in these representations [33, 48, 49]. Specifically, Rho *et al.* use a Discrete Wavelet Transform (DWT) to exploit transform-domain sparsity for compressing feature planes [49]. Li *et al.* repurpose neural image codecs as learned nonlinear transforms: for each scene, they pre-train a plane-based NeRF, then scene-specifically fine-tune a subset of neural codec layers and encode the pretrained feature planes with the fine-tuned codec [33]. Pham *et al.* follow the same two-stage recipe but replace the off-the-shelf codec with lightweight nonlinear transforms designed from scratch [48].

Compared with grid-based NeRFs, applying transform coding to 3DGS is more challenging because 3DGS data

are irregular and unordered. To sidestep these challenges, prior work defers the application of transform coding until the post-training stage, once the 3DGS geometry is fixed. Two main strategies have been explored. First, some methods project 3DGS onto a set of feature planes [42] or adopt a triplane representation [9] to implicitly encode Gaussian attributes [31], then compress the learned planes with standard image or video codecs. Second, other methods treat a pretrained 3DGS model as a point cloud and apply point-cloud attribute transforms such as Graph Fourier transform (GFT) [50] and Region-adaptive Hierarchical Transform (RAHT) [16] to compress the model [26, 56, 61, 63].

The above methods borrow transforms from images, video, or point clouds but apply fixed, linear transforms only after training. This decoupling blocks mutual adaptation between the transform and the 3DGS representation, often limiting R–D performance. In contrast, we propose an end-to-end transform-coding framework that jointly adapts the transform and the 3DGS representation, improving compression performance over post-training transform approaches.